HHS Public Access

Author manuscript

Cell Metab. Author manuscript; available in PMC 2022 February 02.

Published in final edited form as:

Cell Metab. 2021 February 02; 33(2): 270–282.e8. doi:10.1016/j.cmet.2020.11.008.

Intercellular mitochondria transfer to macrophages regulates white adipose tissue homeostasis and is impaired in obesity

Jonathan R. Brestoff[1], **Craig B. Wilen**[2], **John R. Moley**[1], **Yongjia Li**[1], **Wei Zou**[1], **Nicole P. Malvin**[1], **Marina N. Rowen**[1], **Brian T. Saunders**[1], **Hongming Ma**[3], **Madison R. Mack**[3,4,5,6], **Barry L. Hykes Jr.**[1], **Dale R. Balce**[1,7], **Anthony Orvedahl**[8], **Jesse W. Williams**[1], **Nidhi Rohatgi**[1], **Xiaoyan Wang**[1], **Michael R. McAllaster**[1], **Scott A. Handley**[1], **Brian S. Kim**[1,3,4,6], **John G. Doench**[9], **Bernd H. Zinselmeyer**[1], **Michael S. Diamond**[1,3,10], **Herbert W. Virgin**[1,7], **Andrew E. Gelman**[1,11], **Steven L. Teitelbaum**[1,3,^,*]

[1]Department of Pathology and Immunology, Washington University School of Medicine, St. Louis, MO, 63110, USA

[2]Department of Laboratory Medicine and Department of Immunobiology, Yale University School of Medicine, New Haven, CT, USA

[3]Department of Medicine, Washington University School of Medicine, St. Louis, MO, 63110, USA

[4]Center for the Study of Itch, Washington University School of Medicine, St. Louis, MO, 63110, USA

[5]Division of Biology and Biomedical Sciences, Washington University School of Medicine, St. Louis, MO, 63110, USA

[6]Department of Anesthesiology, Washington University School of Medicine, St. Louis, MO, 63110, USA

[7]Vir Biotechnology, San Francisco, CA, 94158, USA

[8]Department of Pediatrics, Washington University School of Medicine, St. Louis, MO, 63110, USA

[9]Broad Institute of MIT and Harvard, Cambridge, MA, 02142, USA

[10]Department of Molecular Microbiology, Washington University School of Medicine, St. Louis, MO, 63110, USA

[*]Correspondence to: teitelbs@wustl.edu.

Author contributions: J.R.B., C.B.W., J.R.M., M.N.R., N.P.M., Y.L., W.Z., H.M, B.T.S., M.R.M., B.L.S., D.R.B., A.O., and J.W.W. performed experiments. J.R.B., C.B.W., J.R.M., H.M., D.B., A.O., B.H.Z., S.A.H., B.S.K., J.D., G.J.R., M.S.D., H.W.V., A.E.G., and S.L.T. designed the project. J.R.B., C.B.W., J.R.M., Y.L., B.T.S., M.R.M., B.L.H. Jr., W.Z., N.R., X.W., B.H.Z., and J.W.W. analyzed the data. J.R.B. wrote the paper. All authors read, edited, and approved the manuscript.

[^]Lead contact

Declaration of Interests: D.R.B. and H.W.V. are employees of Vir Biotechnology, a for-profit institution. M.S.D. is a consultant for Inbios and on the Scientific Advisory Board of Moderna. B.S.K. has served as a consultant for AbbVie, Inc., Concert Pharmaceuticals, Incyte Corporation, Menlo Therapeutics, and Pfizer, Inc; has participated on the advisory board for Celgene Corporation, Kiniksa Pharmaceuticals, Menlo Therapeutics, Regeneron Pharmaceuticals, Inc., Sanofi, and Theravance Pharmaceuticals; is a stockholder of Gilead Sciences, Inc. and Mallinckrodt Pharmaceuticals; and is a Founder and Chief Scientific Officer of Nuogen Pharma, Inc. The other authors declare no competing interests.

[11]Department of Surgery, Washington University School of Medicine, St. Louis, MO, 63110, USA

SUMMARY

Recent studies suggest that mitochondria can be transferred between cells to support the survival of metabolically compromised cells. However, whether intercellular mitochondria transfer occurs in white adipose tissue (WAT) or regulates metabolic homeostasis *in vivo* remains unknown. We found that macrophages acquire mitochondria from neighboring adipocytes *in vivo* and that this process defines a transcriptionally distinct macrophage subpopulation. A genome-wide CRISPR-Cas9 knockout screen revealed that mitochondria uptake depends on heparan sulfate (HS). High fat diet (HFD)-induced obese mice exhibit lower HS levels on WAT macrophages and decreased intercellular mitochondria transfer from adipocytes to macrophages. Deletion of the HS biosynthetic gene *Ext1* in myeloid cells deceases mitochondria uptake by WAT macrophages, increases WAT mass, lowers energy expenditure, and exacerbates HFD-induced obesity *in vivo*. Collectively, this study suggests that adipocytes and macrophages employ intercellular mitochondria transfer as a mechanism of immunometabolic crosstalk to regulate metabolic homeostasis and that is impaired in obesity.

Graphical Abstract

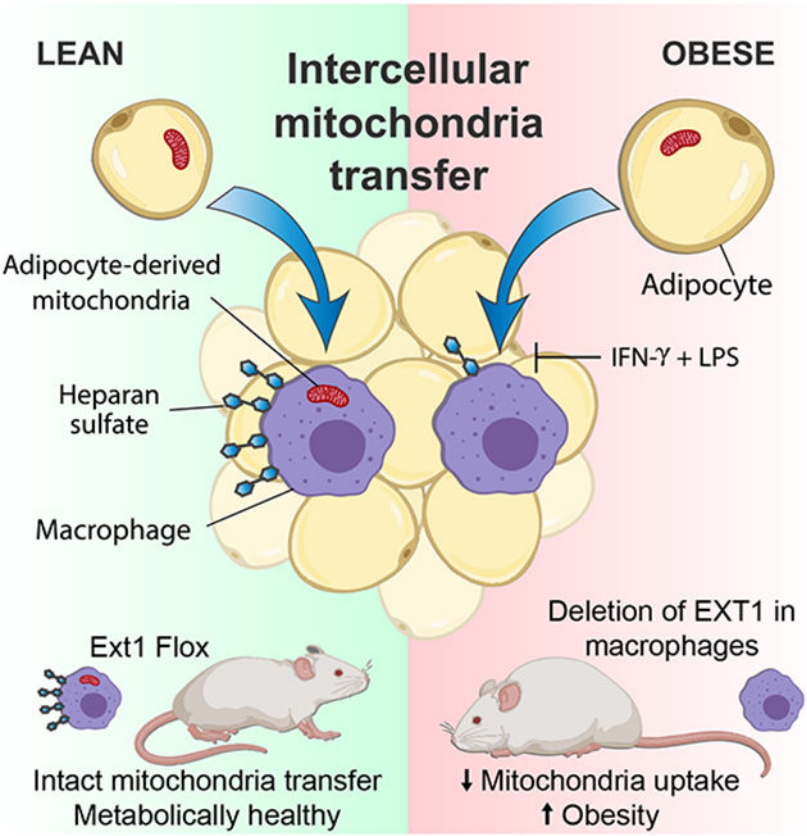

eTOC

Brestoff et al. show that adipose tissue-resident macrophages acquire mitochondria from neighboring adipocytes in a heparan sulfate-dependent process that is impaired in obesity. Genetic disruption of mitochondria uptake by macrophages reduces energy expenditure and exacerbates diet-induced obesity in mice, indicating that intercellular mitochondria transfer to macrophages mediates systemic metabolic homeostasis.

INTRODUCTION

Obesity is an increasingly prevalent metabolic disease that affects 38% of adults and 16% of children and adolescents and is an independent risk factor for the development of many other disorders such as type 2 diabetes, cardiovascular diseases, and cancer (Flegal et al., 2016; Ogden et al., 2016; Patterson et al., 2004). Although obesity pathogenesis is driven by chronic positive energy balance, where caloric intake exceeds caloric expenditure, recent studies have revealed that the immune system modulates neuroendocrine pathways that govern not only food intake but also energy expenditure (Brestoff and Artis, 2015; Lee et al., 2018; Reilly and Saltiel, 2017; Sun et al., 2011; Wellen and Hotamisligil, 2003). In particular, macrophages in white adipose tissue (WAT) regulate metabolic homeostasis by promoting glucose utilization by adipocytes, regulating lipid storage and release, and increasing energy expenditure through modulation of sympathetic tone to WAT (Camell et al., 2017; Flaherty et al., 2019; Pirzgalska et al., 2017; Qiu et al., 2014; Rao et al., 2014; Wu et al., 2011; Wynn et al., 2013). In the context of obesity, various cytokines activate macrophages in WAT to promote a chronic inflammation that dysregulates glucose, lipid, and energy metabolism (Hotamisligil, 2017; Larabee et al., 2020; McLaughlin et al., 2017; Reilly and Saltiel, 2017). Despite these critical advances, we lack a complete understanding of how macrophages and adipocytes interact with each other to maintain metabolic homeostasis.

In 2006, it was reported that mtDNA-deficient ρ^0 cells, which lack functionally competent mitochondria, can capture purified mitochondria from supernatants and that this process promotes cell proliferation (Spees et al., 2006). This phenomenon of mitochondria uptake has been confirmed in various ρ^0 cell lines and can restore normal mitochondrial respiration in ρ^0 cells (Jackson and Krasnodembskaya, 2017; Kim et al., 2018; Sinha et al., 2016). It is known that cells can release functional mitochondria that are then captured by recipient cells (Jiang et al., 2016; Kitani et al., 2014; Maeda and Fadeel, 2014; Scozzi et al., 2019; Torralba et al., 2016). It is also reported that cells can release extracellular vesicles (EVs) that contain mitochondria, with recipient cells acquiring mitochondria through an EV-cell fusion event (Boudreau et al., 2014; Torralba et al., 2016). In both mice and humans, mitochondria and EV-associated mitochondria circulate in blood (Al Amir Dache et al., 2020; Boudreau et al., 2014; Chiu et al., 2003; Pollara et al., 2018; Scozzi et al., 2019). Intercellular mitochondria transfer has been implicated in several disease processes, including ischemic stroke (Hayakawa et al., 2016), inflammatory pain (Raoof et al., 2020), cancer cell growth (Chang et al., 2019; Dong et al., 2017; Griessinger et al., 2017; Rebbeck et al., 2011), acute lung injury repair (Islam et al., 2012), hypoxia-induced pulmonary hypertension (Zhu et al., 2016), and allograft rejection (Lin et al., 2000; Pollara et al., 2018; Scozzi et al., 2019).

However, it remains unknown whether intercellular mitochondria transfer occurs in adipose tissues or whether this process regulates systemic metabolic homeostasis.

Here, we employed an adipocyte-specific mitochondria reporter (MitoFat) mouse and demonstrate that macrophages in WAT acquire mitochondria from adipocytes *in vivo*. This adipocyte-to-macrophage mitochondrial transfer axis defines a distinct macrophage subpopulation in WAT and is severely decreased in high fat diet (HFD)-obesity due to reduced mitochondria uptake by macrophages. A genome-wide CRISPR-Cas9 screen revealed that mitochondria uptake depends on the heparan sulfate (HS) biosynthetic pathway, including the genes *Exostosin 1 (Ext1)* and its heterodimer *Ext2*, which have been linked to the maintenance of glucose and lipid homeostasis in mice and humans (Busse et al., 2007; Liu et al., 2013; Mooij et al., 2015; Sladek et al., 2007). Epididymal (e)WAT macrophage HS levels are decreased in obese mice, and IFN-γ plus LPS treatment downregulates expression of HS synthetic enzymes and impairs mitochondria uptake despite promoting bead phagocytosis. Myeloid cell-specific deletion of *Ext1*, which is required for HS synthesis (Busse et al., 2007; Lin et al., 2000; Sasisekharan and Venkataraman, 2000), impairs mitochondria uptake by macrophages in WAT and leads to dysregulated energy homeostasis characterized by lower energy expenditure, accumulation of WAT mass, glucose intolerance, and increased susceptibility to diet-induced obesity. Collectively, these observations suggest that intercellular mitochondria transfer represents an unappreciated mechanism of cellular communication that may regulate systemic metabolic homeostasis.

RESULTS

Macrophages in white adipose tissue acquire mitochondria from other cell types in vivo

To test whether intercellular mitochondria transfer occurs *in vivo*, we performed bone marrow transplants of congenic CD45.1 wildtype (WT) bone marrow into host CD45.2 mitochondria reporter mice that express the fluorescent protein Dendra2 attached to the mitochondria targeting sequence of cytochrome c, complex VIII (mtD2) (Pham et al., 2012) (Fig. 1A). As a control, WT CD45.1 bone marrow was transplanted into WT CD45.2 recipients. After 12 weeks of engraftment, the stromal vascular fraction (SVF) was isolated from eWAT, inguinal (i)WAT, and brown adipose tissue (BAT) for flow cytometric analysis. The vast majority of the immune cells in these organs were WT donor-derived $CD45.1^+$ $CD45.2^-$ cells, with chimerism of 77% in eWAT, 88% in iWAT, and 72% in BAT (Supplemental Fig. S1A). We then gated on WT $CD45.2^+$ $CD45.1^-$ donor-derived immune cells in eWAT and found that nearly 40% were mtD2+ when isolated from mtD2 hosts (Fig. 1B). The majority of these donor-derived $mtD2^+$ cells were macrophages (65.5%), with other myeloid cells such as monocytes, $CD11c^+$ cells, eosinophils, and neutrophils representing most of the remainder (Fig. 1C, gating strategy shown in Supplemental Fig. S1B). Next, we gated on WT $CD45.1^+$ $CD45.2^-$ $F4/80^+$ $CD64^+$ donor-derived macrophages and found that approximately 60% were $mtD2^+$ when isolated from mtD2 hosts compared to approximately 3% from WT hosts ($P<0.001$, Fig. 1D). The proportion of macrophages that were $mtD2^+$ was significantly higher than that of monocytes, $CD11c^+$ cells, eosinophils, neutrophils, $CD4^+$ cells, or other undefined cell types (Fig. 1E). Further, the proportion of macrophages that are $mtD2^+$ was significantly higher in eWAT and iWAT than in BAT (Fig.

1F). Collectively, these bone marrow transplant data suggest that macrophages in WAT and, to a lesser degree BAT, acquire mitochondria from host cells.

A limitation of flow cytometry is that it cannot distinguish between surface binding and internalization of host cell-derived mitochondria. To determine if mitochondria are internalized *in vivo*, we isolated macrophages from eWAT of WT mice, labelled them with CytoTracker Orange (CMTMR), adoptively transferred these cells into mtD2 host mice, and then performed intravital 2-photon microscopy on host eWAT (Fig. 2A). This imaging technique allowed us to capture images approximately 25-30 μm deep within eWAT of live mice. Host eWAT revealed large adipocytes (dashed circle), host-derived mtD2$^+$ mitochondria, and CMTMR$^+$ donor macrophages adjacent to host adipocytes (Fig. 2B). This indicates that adoptively transferred eWAT macrophages can relocate to their tissue-of-origin, as has been observed with eosinophils (Wu et al., 2011) and group 2 innate lymphoid cells (Brestoff et al., 2015). Critically, CMTMR$^+$ donor macrophages contained internalized host-derived mitochondria and appeared to exhibit interactions with host-derived mitochondria at the plasma membrane (Fig. 2C). Three-dimensional reconstructions with positional mapping confirmed that host cell-derived mitochondria can be found within CMTMR$^+$ donor macrophages (Fig. 2D). In addition, time-lapse videography revealed a mitochondria uptake event, trafficking of host cell-derived mitochondria within CMTMR$^+$ donor macrophages, and apparent fusion and fission involving internalized mitochondria (Fig. 2E and Supplemental Movie S1). These data confirm that macrophages in WAT can internalize mitochondria from other cell types *in vivo*.

Adipocytes transfer mitochondria to macrophages in vivo, defining a distinct macrophage subpopulation

Given the abundance of adipocytes in WAT, we hypothesized that adipocytes might transfer their mitochondria to macrophages. To test this, we generated adipocyte-specific mitochondria reporter mice (MitoFat) by crossing *mtD2$^{Flox/Flox}$* (Pham et al., 2012) to *Adipoq$^{Cre/+}$* mice. We found that approximately 40% of macrophages in gonadal (g)WAT contained mitochondria that were derived from adipocytes (Fig. 3A-3B). To confirm that adipocytes transfer their mitochondria to macrophages, we adoptively transferred CMTMR-labelled eWAT macrophages into MitoFat mice and performed intravital 2-photon microscopy of host eWAT. Three-dimensional reconstructions with positional mapping confirmed that adipocyte-derived mitochondria are within CMTMR$^+$ donor macrophages (Fig. 3C). These observations define an adipocyte-to-macrophage mitochondrial transfer axis that occurs in WAT *in vivo*.

To test whether intercellular mitochondria transfer from adipocytes to macrophages is associated with alterations in the phenotype of WAT macrophages, we isolated WAT SVF from MitoFat mice and directly compared macrophages that had (mtD2$^+$) or had not (mtD2$^-$) received mitochondria from adipocytes (Fig. 3D). First, we found that mtD2$^+$ macrophages had modestly (15%) but significantly higher mitochondrial mass, as indicated by the charge-independent MitoID-Red mitochondria dye, than mtD2$^-$ macrophages from the same samples (Fig. 3E). Overall mitochondrial membrane potential, as indicated by the charge-dependent CMX Rosamine dye, was decreased in mtD2$^+$ versus mtD2$^-$ macrophages

(Fig. 3F). MitoSOX staining, an indicator of mitochondria reactive oxygen species including but not limited to superoxide (Kalyanaraman et al., 2017), was elevated in mtD2$^+$ macrophages compared to mtD2$^-$ macrophages (Fig. 3G). Second, we exposed WAT SVF isolates to 1 μm red fluorescent latex beads and found that mtD2$^+$ macrophages exhibited significantly decreased bead phagocytosis than mtD2$^-$ macrophages from paired samples (Fig. 3H).

Next, we sort-purified mtD2$^-$ and mtD2$^+$ macrophages from eWAT of MitoFat mice and performed unbiased RNA sequencing (Supplemental Table S1). Principal component analyses indicated that eWAT macrophages that had internalized mitochondria from adipocytes were transcriptionally distinct from macrophages that had not taken up mitochondria (Fig. 3I). Differential gene expression analyses showed that 120 genes were significantly downregulated and 219 genes were significantly upregulated at least 2-fold (Fig. 3J). The top 20 differentially expressed genes in mtD2$^+$ vs mtD2$^-$ macrophages included up-regulated mtDNA-encoded, chemokine and anti-inflammatory genes and down-regulated major histocompatibility complex (MHC)-II antigen presentation genes (Supplemental Fig. S2). Further, Gene Set Enrichment Analysis (GSEA) indicated that macrophages which had mitochondria transferred from adipocytes were enriched in genes associated with the Hypoxia inducible factor (HIF)-1α/Tissue factor (TF) pathway (Fig. 3K) and de-enriched for genes associated with electron transport (Fig. 3L) and collagen synthesis (Fig. 3M). Collectively, these data indicate that mitochondria transfer from adipocytes to macrophages defines a distinct macrophage subpopulation.

A genome-wide CRISPR-Cas9 knockout screen identifies the heparan sulfate biosynthetic pathway to be essential for mitochondria uptake

Mitochondria uptake is known to be diminished by various cytochalasins, a family of fungal metabolites that inhibit actin polymerization and the ability to rearrange the cytoskeleton (Boudreau et al., 2014; Kitani et al., 2014). However, little is known about which genes are required for mitochondria uptake. N-formylmethionine residues are found only in bacterial and mtDNA-encoded proteins and bind Formyl peptide receptor 1 (FPR1), a gene that is highly expressed by macrophages (Gemperle et al., 2012; He and Ye, 2017). Therefore, we hypothesized that FPR1 might mediate mitochondria transfer from adipocytes to macrophages. To test this, we crossed MitoFat to *Fpr1*$^{-/-}$ mice to generate FPR1-deficient MitoFat mice and, unexpectedly, found that FPR1 is not required for mitochondria transfer from adipocytes to macrophages *in vivo* (Supplemental Fig. S3). While we cannot exclude a role for other FPR family members in mediating mitochondria transfer, we turned to an unbiased approach to provide further insight into the molecular mechanisms mediating mitochondria uptake by macrophages.

We employed a genome-wide CRISPR-Cas9 knockout screen to identify genes that are essential for mitochondria uptake. To accomplish this, we stably transduced BV2 myeloid cells to express Cas9, introduced the Brie CRISPR library (Doench et al., 2016) with ~4 sgRNA guides targeting each of 19,674 genes (Doench et al., 2016; Orvedahl et al., 2019), and then exposed the pool of cells to mtD2 mitochondria (Fig. 4A and Supplemental Fig. S4A-B). We then sort-purified mtD2$^-$ BV2 cells that failed to physically interact with

exogenous mitochondria (Supplemental Fig. S4B). The sgRNA guides were amplified and sequenced in the mtD2^{-} and input populations, and STARS Score enrichment analysis was performed. This screen identified 23 candidate genes with a false discovery rate (FDR) <0.05, each with a STARS Score >4.5 (Fig. 4B and Supplemental Table S2). Of these 23 genes, 13 are involved in heparan sulfate biosynthesis (Lindahl et al., 2015) (red genes, Fig. 4C), which was confirmed by Gene Ontology (GO) term enrichment analysis that indicated a >200-fold enrichment for genes related to heparan sulfate proteoglycan (HSPG) biosynthetic process (Fig. 4D). These 13 genes traced the entire heparan sulfate biosynthetic process (Lindahl et al., 2015), including the genes required for synthesis of HS substrates (*Uxs1, Ugp2,* and *Ugdh*), the glycosaminoglycan (GAG) linker chain (*Fam20b, B4galt7, B3galt6,* and *B3gat3*), and the HS chain (*Extl3, Ext1,* and *Ext2*), as well as genes involved in HS polymer sulfation (*Papss1, Slc35b2,* and *Hs6st1*) (Fig. 4E).

To validate that heparan sulfates are required for optimal mitochondria uptake, we used CRISPR sgRNA guides directed against *B3gat3, B3galt6, B4galt7, Uxs1, Upg2, Ugdh, Extl3, Ext1, Ext2, Slc35b2, Papss1, Hs6st1* to generate gene-edited clonal cell lines. As a control, we used a CRISPR sgRNA guide against green fluorescent protein (GFP). Each gene-edited cell line had undetectable heparan sulfates on their cell surface, except for sgRNA *Hs6st1,* a cell line that is capable of synthesizing intact heparan sulfate chains but which lacks 6-O sulfation (Fig. 4F and Supplemental Fig. S4C). Each gene-edited cell line exhibited significantly decreased mitochondria uptake compared to control cells (Fig. 4G). In contrast, deletion of these heparan sulfate synthesis genes did not affect uptake of 1 μm latex beads (Fig. 4H), suggesting that heparan sulfates can facilitate interactions with mitochondria but not all foreign objects. Further supporting a role for heparan sulfates in mitochondria uptake, we found that enzymatic removal of heparan sulfates on BV2 cells with Heparanases I-III impaired mitochondria uptake (Fig. 4I). Consistent with these data, pre-treating purified mitochondria with heparan sulfate proteoglycan (HSPG) inhibited their uptake by BV2 cells *in vitro* (Fig. 4J). In addition, treating MitoFat mice with unfractionated heparin, a highly sulfated form of heparan sulfate that is widely used clinically as an anticoagulant (Oduah et al., 2016), inhibited mitochondria transfer from adipocytes to macrophages in eWAT *in vivo* (Fig. 4K). These genetic, enzymatic, and pharmacological approaches collectively indicate that heparan sulfates are essential for efficient mitochondria uptake both *in vitro* and *in vivo*.

Obesity is associated with decreased mitochondria transfer from adipocytes to macrophages

To test whether intercellular mitochondria transfer from adipocytes to macrophages is altered in the setting of obesity, we fed MitoFat mice a normal chow or high fat diet (HFD) for 12 weeks. HFD-induced obesity was associated with marked decrease in intercellular mitochondria transfer from adipocytes to macrophages in WAT (Fig. 5A-5B). To test whether this obesity-associated change is due to impaired release of mitochondria from adipocytes, impaired uptake of mitochondria by macrophages, or both, we utilized a WAT explant co-culture system. Specifically, minced WAT explants from CD45.1 mtD2 mice fed a chow or HFD for 10-12 weeks were co-cultured with minced WAT explants from CD45.2 WT mice fed a chow or HFD for 10-12 weeks. Flow cytometry was used to determine the

proportion of CD45.2 WT macrophages that had received mitochondria from mtD2 donor WAT. We found that varying the nutritional status of the donor mtD2 WAT had no effect on mitochondria transfer to recipient macrophages (Fig. 5C). In contrast, we observed significantly decreased mitochondria transfer from chow-fed mtD2 WAT to macrophages from HFD WAT (Fig. 5C). Thus, the decrease in mitochondria transfer from adipocytes to macrophages appears to be due to a macrophage-intrinsic impairment in mitochondria uptake. Consistent with this result, we observed that eWAT macrophages from HFD-fed mice have substantially decreased levels of HS on their surface compared to normal chow-fed controls (Fig. 5D).

In obesity, pro-inflammatory cytokines such as IFN-γ, LPS, and other stimuli promote the accumulation of M1-like macrophages in WAT (Brestoff and Artis, 2015; Caesar et al., 2012; Cani et al., 2007; Clemente-Postigo et al., 2019; Hotamisligil, 2017; Lee et al., 2018). We found that the proportion of F4/80$^+$ CD64$^+$ CD206$^-$ CD11c$^+$ (M1-like) macrophages that had received mitochondria from adipocytes was significantly lower than in F4/80$^+$ CD64$^+$ CD206$^+$ CD11c$^-$ (M2-like) macrophages in mice fed a chow diet (Fig. 5E). Further, both M1-like and M2-like WAT macrophage populations exhibited a decrease in the proportion of mtD2$^+$ cells in the setting of HFD-induced obesity (Fig. 5E), and the percentage of mtD2+ macrophages correlated with cell surface HS levels (Fig. 5F). Therefore, we hypothesized that M1-like polarization with IFN-γ and LPS might impair mitochondria uptake. To test this idea, we polarized BV2 cells towards an M0, M2, or M1 phenotype with phosphate buffered saline (PBS), IL-4, or IFN-γ plus LPS, respectively, for 24 hours. Polarization was confirmed by intracellular flow cytometric analysis of the M2 marker arginase 1 (ARG1, Supplemental Fig. S5A) and the M1 marker inducible nitric oxide synthase (iNOS) (Supplemental Fig. S5B). We then cultured M0-, M1-, and M2-polarized BV2 cells with 1 μm red latex beads, which are similar in size to mitochondria, and found that IFN-γ and LPS treatment resulted in increased bead phagocytosis compared to IL-4 (Fig. 5G and Supplemental Fig. S5C). This observation is consistent with prior studies showing that activation of macrophages with IFN-γ increases both phagocytosis and macropinocytosis (Bosedasgupta and Pieters, 2014). In contrast, treatment of BV2 cells with IFN-γ plus LPS markedly decreased uptake of mitochondria, whereas IL-4 had no effect (Fig. 5H and Supplemental Fig. S5D). We also found that IFN-γ plus LPS decreased the expression of transcripts involved in HS biosynthesis, whereas IL-4 had no effect (Fig. 5I). These data indicate that IFN-γ plus LPS activation impairs mitochondria uptake and suggest that these pro-inflammatory stimuli may contribute to the reduction in adipocyte-to-macrophage mitochondria transfer observed in murine obesity.

Genetic deletion of Ext1 from myeloid cells impairs mitochondria transfer to macrophages and promotes fat accumulation

To investigate the role of intercellular mitochondria transfer in regulating systemic metabolism, we conditionally deleted *Ext1* from myeloid cells using *Lyz2*-Cre. Deletion of *Ext1* in macrophages did not affect the frequencies (Fig. 6A) and numbers (Fig. 6B) of macrophages in eWAT. This indicates that *Ext1* is dispensable for maintaining macrophage abundance in chow-fed mice. Next, we confirmed that eWAT macrophages from *Ext1*$^{\Delta Lyz2}$ mice had reduced levels of heparan sulfates on their surface (Fig. 6C) and impaired

mitochondria uptake (Fig. 6D) compared to $Ext1^{F/F}$ littermate controls. Moreover, we found that $Ext1^{\Delta Lyz2}$ mice had significantly higher body weight (Fig. 6E), absolute eWAT mass (Fig. 6F), and relative eWAT mass normalized to body weight (Fig. 6G) compared to $Ext1^{F/F}$ littermate controls. Whole body lean mass did not differ $Ext1^{\Delta Lyz2}$ and $Ext1^{F/F}$ groups, however whole body fat mass (Fig. 6H) and adiposity (Fig. 6I) were significantly increased in $Ext1^{\Delta Lyz2}$ mice. These changes were accompanied by impaired glucose tolerance (Fig. 6J) and insulin tolerance (Fig. 6K) in $Ext1^{\Delta Lyz2}$ mice compared to controls.

These observations suggested that $Ext1^{\Delta Lyz2}$ mice have altered energy homeostasis. To investigate this hypothesis, we performed metabolic cage analyses and found that $Ext1^{\Delta Lyz2}$ mice exhibited significantly lower energy expenditure than $Ext1^{F/F}$ littermates on a chow diet (Fig. 7A and Fig. 7B). The respiratory quotient (RQ) did not differ between the two groups (Fig. 7C), indicating that energy substrate utilization may be unaltered in $Ext1^{\Delta Lyz2}$ mice. Furthermore, food intake (Fig. 7D) and physical activity (Fig. 7E) also did not differ between the two groups. Given these findings, we hypothesized that $Ext1^{\Delta Lyz2}$ mice would exhibit more severe diet-induced obesity. Indeed, we found that $Ext1^{\Delta Lyz2}$ mice exhibited increased body weight (Fig. 7F) as well as eWAT and iWAT masses (Fig. 7G) following 8 weeks of HFD feeding compared to $Ext1^{F/F}$ littermates. BAT masses did not differ significantly between groups (Fig. 7G). In addition, HFD feeding resulted in more severe glucose intolerance in $Ext1^{\Delta Lyz2}$ mice compared to $Ext1^{F/F}$ controls (Fig. 7H). Taken together, these data indicate that conditional deletion of *Ext1* in myeloid cells impairs mitochondria transfer and decreases energy expenditure, promoting the accumulation of fat mass, promoting the accumulation of fat mass.

DISCUSSION

Here, we provide evidence that adipocytes transfer their mitochondria to macrophages in WAT *in vivo* and that this process defines a transcriptionally distinct macrophage subpopulation. We also demonstrate that this process is decreased in the context of diet-induced obesity due to reduced mitochondria uptake by WAT macrophages. Mitochondria uptake is mediated by HS, and surface levels of HS are decreased on WAT macrophages from obese mice and in BV2 cells following stimulation with IFN-γ and LPS. Furthermore, conditional deletion of EXT1 in myeloid cells reduces WAT macrophage HS levels, impairs mitochondria uptake, promotes fat mass accumulation, and reduces systemic energy expenditure without affecting food intake or physical activity levels.

Previous studies have demonstrated that mitochondria are released by various cell types *in vitro* and *in vivo* and that functional mitochondria circulate in murine and human peripheral blood (Al Amir Dache et al., 2020; Boudreau et al., 2014; Chiu et al., 2003; Maeda and Fadeel, 2014; Pollara et al., 2018; Scozzi et al., 2019; Torralba et al., 2016). It also has been reported that mitochondria-deficient cell types can capture purified mitochondria from their environment and utilize them to support cellular metabolic demands and cell proliferation (Kim et al., 2018; Kitani et al., 2014; Spees et al., 2006). *In vivo*, cancer cells including a mitochondria-deficient ρ^0 melanoma cell line can acquire mitochondria from host cells (Dong et al., 2017; Rebbeck et al., 2011), and ischemic neurons acquire mitochondria from astrocytes in the brain in a murine model of ischemic stroke (Hayakawa et al., 2016). These

and other observations have led to the hypothesis that intercellular mitochondria transfer may serve as a mechanism to rescue or sustain metabolically compromised cells (Torralba et al., 2016). In our studies, macrophages that have acquired mitochondria from adipocytes appear to produce more mitochondrial ROS and exhibit evidence of hypoxia and de-enrichment of nuclear-encoded genes involved in mitochondrial homeostasis and maintenance of the electron transport chain. Although deletion of *Ext1* from myeloid cells impaired mitochondria uptake by WAT macrophages without affecting macrophage abundance at steady state, further research is needed to determine whether and how mitochondria transfer affects nuclear gene expression and supports the metabolic demands of macrophages.

Emerging evidence supports a role for intercellular mitochondria transfer in regulating the immune system. For example, the capture of exogenous mitochondria is reported to promote regulatory T cell programming at steady state, suggesting that mitochondria transfer might have anti-inflammatory properties (Court et al., 2020). In contrast, mitochondria capture by neutrophils promotes pulmonary inflammation following lung transplantation (Scozzi et al., 2019). Our studies indicate that mitochondria uptake by macrophages occurs in WAT frequently in healthy conditions when macrophages are polarized towards an M2-like activation state driven by type 2 cytokines, such as IL-4 and IL-13, which are produced by group 2 innate lymphoid cells, eosinophils, and other cell types present in healthy WAT (Brestoff and Artis, 2015; Lee et al., 2018). In comparison, the frequency of mitochondria transfer from adipocytes to macrophages is markedly decreased in obesity, a pro-inflammatory state in which macrophages are exposed to factors that induce a type 1 immune response, including but not limited to IFN-γ and LPS (Brestoff and Artis, 2015; Caesar et al., 2012; Cani et al., 2007; Clemente-Postigo et al., 2019; Hotamisligil, 2017; Makki et al., 2013; Reilly and Saltiel, 2017). This suggests that M1-like polarization inhibits mitochondria uptake. Consistent with this, the frequency of mitochondria transfer from adipocytes to $CD206^{+}$ $CD11c^{-}$ (M2-like) macrophages is higher than to $CD206^{-}$ $CD11c^{+}$ (M1-like) macrophages, and HFD-induced obesity is associated with decreased mitochondria transfer from adipocytes to both macrophage populations. Further, BV2 cells also exhibit decreased mitochondria uptake following IFN-γ and LPS stimulation. These observations implicate a reduction in mitochondria transfer to be a feature of metabolic diseases such as obesity, at least in WAT.

The mechanisms by which mitochondria are taken up into cells are not well understood. Mitochondria uptake is inhibited by cytochalasins, which impair actin cytoskeleton rearrangement (Boudreau et al., 2014; Kitani et al., 2014). However, there is no known receptor for intact mitochondria. Our genome-wide CRISPR-Cas9 knockout screen identified 23 candidate genes that might contribute to mitochondria uptake. Of these, 13 genes traced the heparan sulfate biosynthesis pathway in an unsupervised analysis, strongly implicating heparan sulfate as an attachment factor to support mitochondria uptake. Deletion of these heparn sulfate biosynthesis genes impaired mitochondria uptake by BV2 cells *in vitro* without affecting phagocytosis of latex beads of a similar size as mitochondria. This suggests that heparan sulfate species may confer some specificity to bind mitochondria but not to all foreign objects. Further supporting a role for HS in mitochondria uptake, stimulating BV2 cells with IFN-γ and LPS downregulated expression of *Ext2* and *Hs6st1,*

genes that are required for HS synthesis and 6-O sulfation, respectively, and eWAT macrophages from HFD-induced obese mice had lower surface HS levels than chow diet-fed controls. The degree of mitochondria transfer from adipocytes to macrophages is correlated with macrophage HS levels. In addition, heparin treatment was sufficient to inhibit mitochondria transfer from adipocytes to macrophages *in vivo*, and conditional deletion of *Ext1* from myeloid cells in mice reduced eWAT macrophage HS levels and mitochondria uptake by WAT macrophages. These data support a role for HS in mediating mitochondria uptake by murine macrophages *in vitro* and *in vivo*. These observations raise questions about whether treating patients with heparin for anti-coagulation results in impaired intercellular mitochondria transfer. Heparin is known to cause metabolic derangements (Lee et al., 1988; Rutstein et al., 1969; Zhu et al., 2017) and reduce inflammation (Ekre et al., 1992; Mousavi et al., 2015) in mice and humans, and further research is needed to determine whether intercellular mitochondria transfer contributes to these effects. Further research will also be needed to determine whether HS mediates mitochondria transfer or obesity pathogenesis in humans and whether other factors or genes are also required for mitochondria uptake or transfer.

The generation of $Ext1^{\Delta Lzy2}$ mice allowed us to investigate whether genetic disruption of mitochondria transfer affects macrophage abundance or systemic metabolism. We found that mice lacking *Ext1* in myeloid cells had unaltered macrophage frequencies or numbers in WAT, suggesting that HS and mitochondria transfer is not required to sustain WAT macrophage abundance. However, $Ext1^{\Delta Lzy2}$ mice exhibited mildly increased body weight and an approximately 30% increase in absolute and relative eWAT mass relative to littermate controls. Metabolic cage analyses indicated that conditional deletion of *Ext1* in myeloid cells resulted in substantially lower energy expenditure without affecting food intake or physical activity, establishing positive energy balance that favors accumulation of fat mass over time. Thus, it appears that intercellular mitochondria transfer to macrophages might contribute to the maintenance of energy homeostasis in mice. These data further raise the possibility that the obesity-associated decrease in mitochondria transfer from adipocytes to macrophages might have a role in weight gain or the metabolic dysfunction in response to a HFD. Additional research will be needed to understand how mitochondria transfer affects macrophage function and WAT and BAT homeostasis.

Interactions between adipocytes and immune cells are essential to maintain metabolic homeostasis and, when dysregulated, can drive pathologic inflammation that promotes obesity and obesity-associated metabolic dysfunction (Brestoff and Artis, 2015; Lee et al., 2018; Singer and Lumeng, 2017; Sun et al., 2011). Here, we identified that intercellular mitochondria transfer occurs *in vivo* in WAT and defined an adipocyte-to-macrophage mitochondria transfer axis that is dysregulated in obesity due to classical or M1-like macrophage polarization. Intercellular mitochondria transfer occurs, at least in part, through a heparan sulfate-dependent mechanism both *in vitro* and *in vivo*, and genetic disruption of HS synthesis on macrophages impairs intercellular mitochondria transfer and compromises energy homeostasis, raising the possibility of a functional relationship. Indeed, patients and mice with heterozygous loss-of-function mutations in the HS synthesis gene *Ext1* have impaired lipid and glucose homeostasis (Mooij et al., 2015). Furthermore, genome-wide association studies have linked single nucleotide polymorphisms in *Ext2*, which forms a

heterodimer with EXT1 to polymerize the heparan sulfate chain (Busse et al., 2007), to increased risk for type 2 diabetes (Sladek et al., 2007). Thus, our findings reveal a new paradigm of immunometabolic cross-talk in which some cells, such as adipocytes, transfer their mitochondria to macrophages to regulate systemic metabolic homeostasis. These observations suggest that intercellular mitochondria transfer may have evolved as a homeostatic process that enables immune cells to respond to and regulate their local tissue microenvironment. Therapeutically targeting intercellular mitochondria transfer may represent an unappreciated strategy to ameliorate metabolic diseases.

Limitations of Study

A significant limitation of these studies is that they were done in mice and cells isolated from mice, not humans. Improved tools and techniques to study intercellular mitochondria transfer in humans, especially *in vivo*, are needed to determine the translational relevance of intercellular mitochondria transfer in the context of human metabolic homeostasis, immunity, obesity pathogenesis, or other disease states. Furthermore, it remains unknown whether intercellular mitochondria transfer to macrophages affects the bioenergetic or metabolic status of the recipient cell, a topic that warrants further study. Although we identify a role for heparan sulfates in mediating intercellular mitochondria transfer *in vitro* and *in vivo* in mice, targeting the heparan sulfate pathway with pharmacologic, enzymatic, and genetic approaches resulted in a partial disruption in mitochondria uptake. This may have impacted the severity of the metabolic abnormalities observed in mice with conditional deletion of *Ext1* in myeloid cells and suggests that there are likely other factors and/or genes that also facilitate the mitochondria uptake process.

STAR METHODS:

Resource Availability

Lead Contact—Requests for resources and reagents should be directed to and will be fulfilled by the Lead Contact, Steven L. Teitelbaum (teitelbs@wustl.edu).

Materials Availability—All reagents are available from the Lead Contact under a material transfer agreement with Washington University in St. Louis.

Data and Code Availability—All data and code to understand and assess the conclusion of this research are available in the main text, supplementary materials, or GEO Database (accession number GSE157462).

Experimental Model and Subject Details

Mouse Models—C57BL/6J (stock number 664), CD45.1 (*Ptprc*^{a}; stock number 2014), *mtDendra2* (PhAM, referred to here as mtD2; stock number 18397), *mtDendra2*$^{Flox/+}$ (PhAM Flox; referred to here as *mtD2*$^{F/+}$ stock number 18385), *Adipoq*$^{Cre/+}$ (stock number 28020), *Fpr1*$^{-/-}$ (stock number 32933), *Ext1*$^{Flox/+}$ (stock no 9326), and *Lyz2*$^{Cre/+}$ (stock no 4781) mice were obtained from Jackson Laboratories (Bar Harbor, Maine). All mice were maintained on a C57BL/6J background, except *Ext1*$^{Flox/Flox}$ and *Ext1*$^{Flox/Flox}$;*Lyz2*$^{Cre/+}$ which were maintained on a mixed C57BL/6J;129 background and used as littermates.

mtD2$^{Flox/+}$ mice express mtD2 under control of a ROSA26 Flox-STOP-Flox system, enabling expression of mtD2 in cells that express Cre recombinase. *mtD2*$^{Flox/Flox}$ mice were crossed with *Adipoq*$^{Cre/+}$ mice to generate *mtDendra2*$^{Flox/+}$ *Adipoq*$^{Cre/+}$ (MitoFat) and *mtDendra2*$^{Flox/+}$ (control) mice. MitoFat mice were also crossed onto an *Fpr1*$^{-/-}$ background. mtD2 mice were crossed to CD45.1 mice to generate CD45.1 mtD2 mice. Mice were genotyped using primers and protocols obtained from Jackson Laboratories or by Transnetyx. Mice were male or female, as indicated, and were age 6-26-weeks-old. All mice had *ad libitum* access to food water and were maintained in a specific-pathogen free facility with a 12h:12h light:dark cycle. Animals were randomly assigned to n=3-8 mice/group per experiment, except where indicated otherwise, and data represent at least 2 independent experiments throughout. Mice were euthanized for tissue harvest using carbon dioxide asphyxiation. All experiments were carried out under the guidelines of the Institutional Animal Care and Use Committee (IACUC) at Washington University in St. Louis and were performed under IACUC-approved protocols.

Cell Culture—BV2 microglia-derived cells (Orchard et al., 2016) were cultured in Delbuco's Modified Eagle Media (DMEM) with 4.5 g/L D-glucose, L-glutamine, and no sodium pyrophosphate (Gibco) that was additionally supplemented with 10% heat-inactivated fetal bovine serum (FBS), 2 mM L-glutamine, 100 U/mL Penicillin, and 100 U/mL Streptomycin (BV2 Media) and maintained at 37 °C with 5% CO_2. BV2 cells (1.0-2.0 x 10^6) were seeded in 150 mm tissue culture-treated polystyrene plates, grown to ~80% confluence over 2-3 days before use or additional passaging.

Method Details

Bone marrow chimeras—Male, 8-week-old mtD2 mice and C57BL/6J mice were lethally irradiated with 1,000 rad and one day later transplanted with 5.0 x 10^6 bone marrow cells isolated from CD45.1 wildtype mice by intravenous administration. Bone marrow cells were isolated from the tibias and femurs and pooled from 5 mice. Recipient mice were allowed to engraft for 12 weeks before euthanization and tissue harvest.

Metabolic cage analyses—*Ext1*$^{Flox/Flox}$*;Lyz2*$^{Cre/+}$ mice and *Ext1*$^{Flox/Flox}$ littermate control males (age 22-26 weeks old) were weighed and placed single-housed in a 16-metabolic cage Comprehensive Laboratory Animal Monitoring System (CLAMS) metabolic cages (Columbus Instruments, Columbus, OH). Mice were acclimated for approximately 16 hours followed by measurement for 24 hours from 07:00 (Zeitgeber time 0hr) to 06:59 the next day (Zeitgeber time 24hr). Mice were housed at room temperature on a 12h:12h light:dark cycle and arrayed in a staggered fashion to equally distribute the two groups from top to bottom and left to right. Mice had *ad libitum* access to food and water (hanging feeders and water bottles on load cells). Cumulative food intake over the 24 hr measurement period was determined. Activity was monitored using infrared laser/detector arrays on the X- and Y-axes. Oxygen consumption and carbon dioxide production were measured by indirect calorimetry using a zirconia O_2 sensor and CO_2 sensor at air flow rates of 0.90 L/min (18 sec line bleed followed by 2 sec measurement for each cage). Cages were measured individually in series (~5.5 min for each complete interval), with room air sampled between each interval to calculate O_2 consumption and CO_2 production. Heat was normalized to

body weight. Data from 2 independent experiments were pooled for analysis with n=16 *Ext1*$^{Flox/FIox}$;*Lyz2*$^{Cre/+}$ mice and n=15 *Ext1*$^{Flox/Flox}$ littermate controls from 7 litters.

Heparin treatment—PBS or Grade I-A unfractionated heparin sodium salt (5 mg/kg body weight, equivalent to 900 U/kg; Sigma-Aldrich) in PBS were administered by intraperitoneal injection to MitoFat or *mtD2*$^{Flox/+}$ control mice daily for 7 days at approximately 5:00 P.M. On the morning of day 7, an additional bolus of PBS or heparin was administered 30 min prior to tissue harvest for flow cytometric analysis.

Glucose homeostasis analyses—All blood glucose concentrations were measured using a Contour (Bayer) handheld glucometer with small droplets of blood obtained from the tail vein. For glucose tolerance tests (GTT), mice were fasted for 16 hours and then fasting blood glucose concentrations were determined and assigned as time point 0 min. A bolus of glucose (1 g glucose/kg body weight) in 0.45% saline was administered by intraperitoneal injection, and blood glucose concentrations were measured in duplicate or triplicate 20, 40, 60, 90, and 120 min later. For insulin tolerance tests (ITT), mice were fasted for 4 hours and then fasting blood glucose concentrations were determined and assigned as time point 0 min. A bolus of human insulin (Humulin R, 0.5 U/kg body weight) in 0.9% saline was administered by intraperitoneal injection, and blood glucose concentrations were measured in duplicate or triplicate 20, 40, and 60 min later.

Body composition analysis—Mice were weighed, and body composition was measured using an EchoMRI-100H 2n1 with a horizontal probe configuration (EchoMRI, Houston, TX).

Isolation of immune cells from mouse tissues—Epididymal white adipose tissue (eWAT), ovarian (o)WAT, inguinal (i)WAT, and/or brown adipose tissue (BAT) were finely minced and digested with 0.1% collagenase type II (Sigma-Aldrich, C6885) in DMEM at 37 °C for 60 min in an orbital shaker with rotation at 200 rpm while tilted at a 45° angle. Single cell suspensions of eWAT, iWAT, or BAT were passed through a 100 μm nylon mesh filter, washed with 10 mL of Wash Media (DMEM with 5% FBS, 2 mM L-glutamine, and 100U/mL Penicillin-Streptomycin), and centrifuged at 500 x *g* for 5 min at 4 °C. The floating adipocytes were aspirated and the stromal vascular fraction (SVF) pellet was resuspended in 1 mL ACK Red Blood Cell (RBC) Lysis Buffer (Gibco). After 3-5 min at room temperature, the RBC lysis reaction was quenched with 10 mL Wash Media, the cells were pelleted as above, and the pellet was resuspended in Wash Media for subsequent staining for flow cytometric analyses.

Flow cytometry and cell-sorting—Cells were washed in 200 μL PBS and then stained in 50 μL of ZombieUV (1:600, BioLegend) in PBS and incubated on ice for 10 min covered in foil. The reaction was quenched with 200 μL of FACS Buffer (PBS supplemented with 2.5% heat-inactivated PBS and 2 mM EDTA), and cells were pelleted as above. Cells were resuspended in 50 μL of 10 μg/mL FcBlock (rat anti-mouse CD16/32, clone 2.4G2, BD Biosciences) for 10 min covered in foil before addition of 50 μL 2X stain cocktail (final concentration 1X, see below for antibody information and final dilutions) comprised of various fluorophore-conjugated antibodies in Brilliant Stain Buffer (BD Biosciences)

containing 10 μg/mL FcBlock. Cells were stained for 20-30 min on ice covered in foil and then washed 3 times in 200 μL FACS Buffer. After the final resuspension, 25 μL CountBright Absolute Counting Beads (ThermoFisher) were added for enumeration of cell numbers. For intracellular cytokine staining of BV2 cells with anti-ARG1-APC and anti-iNOS-PE/Cy7 (details below), cells were incubated with FcBlock as above and then fixed in 100 μL of CytoFix/CytoPerm Buffer (BD Biosciences) for 30 min on ice while covered in foil. Cells were washed 3 times in 200 μL of CytoPerm Wash (1X) per manufacturer's instructions and then stained in 1X CytoPerm Wash containing fluorophore-conjugated antibodies and 10 μg/mL FcBlock for 1 hour on ice while covered in foil. Cells were washed 3 times in 200 μL of CytoPerm Wash (1X), washed once in 200 μL of FACS Buffer, and then resuspended in FACS Buffer for flow cytometry.

The following antibodies were used: rat anti-mouse SiglecF-PE (BD Pharmingen; clone E50-2440; 1:400), rat-anti-mouse F4/80-PE (BioLegend; clone BM8; 1:300), mouse anti-mouse CD64-PE-Dazzle594 (BioLegend; clone X54-5/7.1; 1:300), rat anti-mouse CD206-PE/Cy7 (BioLegend; clone C068C2; 1:200), rat anti-mouse iNOS-PE/Cy7 (eBioscience; clone CXNFT; 1:200), rat IgG2a kappa-PE/Cy7 (eBiosceince; clone eBR2a; 1:200), rat anti-mouse CD45.1-APC (BioLegend; clone A20; 1:200), rat anti-mouse F4/80-APC (BioLegend; clone BM8; 1:300), rat anti-mouse/human ARG1-APC (eBioscience; clone A1exF5; 1:200), rat IgG2a kappa-APC (eBioscience; clone BR2a; 1:200), rat anti-mouse CD4-APC/Fire750 (BioLegend; clone RM4-5; 1:300), rat anti-mouse CD45-BUV395 (BD Horizon; clone 30-F11; 1:200), rat anti-mouse CD45.2-BUV395 (BD Horizon; Clone 104; 1:200), rat anti-mouse SiglecF-BV421 (BD Pharmingen; clone E50-2440; 1:400), rat anti-mouse Ly6C-BV510 (BioLegend; clone HK1.4; 1:400), rat anti-mouse Ly6G-BV785 (BioLegend; clone 1A8; 1:300), and rat anti-mouse/human CD11b-BV650 (BioLegend; clone M1/70; 1:400). For heparan sulfate (HS) quantification on cells, cells were stained with or without mouse anti-HS IgM antibody (amsbio; clone F58-10E4; 1:100) followed by a rat anti-mouse IgM-PE/Cy7 secondary antibody (BioLegend; clone RMM-1; 1:200).

All flow cytometry was performed on a 5-laser BD X20 or flow cytometer. Flow cytometric analyses were performed with FlowJo (version 10, Ashland, OR), and cells were gated on singlets and live cells. Macrophages were defined as $CD45^+$ $SiglecF^-$ $CD11b^+$ $F4/80^+$ $CD64^+$ cells. Monocytes were defined as $CD45^+$ $SiglecF^-$ $F4/80^+$ $Ly6C^{hi}$ cells. Eosinophils were defined as $SiglecF^+$ SSC^{hi} cells. Neutrophils were defined as $CD11b^+$ $Ly6G^+$ cells. Cell sorting of eWAT macrophages was performed on a BD Aria, and cells were sorted directly into RLT Buffer and then frozen on dry ice and stored at −80 °C until RNA extraction using the RNeasy Micro Kit (Qiagen).

Staining eWAT macrophages with mitochondria dyes—eWAT SVF cells were isolated from male WT or MitoFat mice age 10-12 weeks old, as described above. Cells from 2 eWAT pads per mouse were resuspended in 400 μL Wash Media and divided into 4 equal aliquots. To the aliquots were resuspended in 200 μL Wash Media (unstained control) or 200 μL Wash Media containing MitoID-Red (1:10,000 dilution; Enzo Life Sciences), CMX Red Rosamine (100 nM; ThermoFisher), or MitoSOX Red (5 μM; ThermoFisher) per manufacturer protocols. Cells were incubated at 37°C with 5% CO_2 for 15 min and then

washed with 200 μL Wash Media twice and 200 μL PBS before staining for flow cytometric analysis, as described above.

Adoptive cell transfer—eWAT SVF was obtained from n=3 C57BL/6J mice as described above and pooled for each independent experiment. RBC-depleted SVF cells were washed in 1 mL MACS Buffer (PBS containing 1% bovine serum albumin and 1 mM EDTA) and pelleted by centrifugation at 500 x *g* for 5 min at 4 °C. The cells were resuspended in 90 μL of MACS Buffer followed by addition of 10 μL magnetic nanobeads conjugated to anti-F4/80 antibody (Miltenyi Biotec). After a 15-min incubation at 4 °C covered in foil, the SVF cells were passed through a 30 μm nylon mesh and then an LS Column on a QuadroMACS magnet (Miltenyi Biotec). Cells were washed 3 times with 3 mL of MACS Buffer and then eluted in 5 mL MACS Buffer. Purity was confirmed by flow cytometry and was >95%. The cells were pelleted by centrifugation at 500 x *g* for 5 min at 4 °C, and the cells were resuspended in 2 mL Wash Buffer containing 10 μM CytoTracker Orange (also known as CMTMR; ThermoFisher; stock solution 10 mM in DMSO) and incubated at 37 °C for 30 min. The CMTMR-labelled cells were washed 2 times in 25 mL Wash Media and one time in 25 mL PBS. The washed cell pellet was resuspended in 300 μL PBS for cell counting. Cells (approximately 5 x 10^4 per mouse) were administered by intraperitoneal injection into male or female mtD2 mice or male MitoFat mice and then imaged by intravital 2-photon microscopy 1-3 days after the adoptive transfer.

Intravital 2-photon microscopy—Mice were anesthetized by intraperitoneal injection of ketamine (50 mg/kg) and xylazine (10 mg/kg) and maintained with halved doses administered every hour. The mouse lower abdomen was carefully shaved with Nair (Church & Dwight Co.) and washed with PBS to remove the excess lotion. A small incision was made in the lower abdomen in order to expose the eWAT pad which was kept moist with PBS and carefully positioned under a coverslip that was screwed into place for imaging. During the acquisition, mouse status was closely monitored. Images were collected using a customized Leica SP8 2-photon microscope equipped with a 25X/0.95 NA water-dipping objective and a Mai Tai HP DeepSee Laser (Spectra-Physics) tuned to 880 nm. Fluorescence emission was separated by 3 high-efficiency dichroic mirrors cutting at 458, 495, and 560 nm (Semrock) and directly directed to 4 supersensitive external detectors. These detectors and a resonant galvo scanner with 12,000 Hz frequency very short dwell times under relatively low laser power. This prevents photo-conversion of the Dendra2 protein. 3D stacks consisting of between 21 and 31 planes (0.5 μm step size) were captured every 30 seconds. Imaris software (BITPLANE, Inc.) was used to reconstruct 3-dimmensional (3-D) images, determine cellular localization with 3-D positional mapping, and generate movies derived from time-lapsed imaging.

RNA sequencing and analysis—RNA was extracted from sort-purified macrophages (see above) using Qiagen RNeasy Micro kit with on-column DNase I (Qiagen) digestion and then eluted in 14 μL RNase/DNase-free water. Samples were prepared according to library kit manufacturer's protocol, indexed, pooled, and sequenced on an Illumina HiSeq. Basecalls and demultiplexing were performed with Illumina's bcl2fastq software and a custom python demultiplexing program with a maximum of one mismatch in the indexing

read. RNA-seq reads were then aligned to the Ensembl release 76 top-level assembly with STAR version 2.0.4b (Dobin et al., 2013). Gene counts were derived from the number of uniquely aligned unambiguous reads by Subread:featureCount version 1.4.5 (Liao et al., 2014). Isoform expression of known Ensembl transcripts were estimated with Sailfish version 0.6.13 (Patro et al., 2017). Sequencing performance was assessed for the total number of aligned reads, total number of uniquely aligned reads, and features detected. The ribosomal fraction, known junction saturation, and read distribution over known gene models were quantified with RSeQC version 2.3 (Wang et al., 2012).

All gene counts were then imported into the R/Bioconductor package EdgeR (Robinson et al., 2010) and TMM normalization size factors were calculated to adjust for samples for differences in library size. Ribosomal genes and genes not expressed in the smallest group size minus one samples greater than one count-per-million were excluded from further analysis. The TMM size factors and the matrix of counts were then imported into the R/Bioconductor package Limma (Ritchie et al., 2015). Weighted likelihoods based on the observed mean-variance relationship of every gene and sample were then calculated for all samples with the voomWithQualityWeights (Liu et al., 2015). The performance of all genes was assessed with plots of the residual standard deviation of every gene to their average log-count with a robustly fitted trend line of the residuals. Differential expression analysis was then performed to analyze for differences between conditions and the results were filtered for only those genes with Benjamini-Hochberg false-discovery rate adjusted p-values less than or equal to 0.05.

For each contrast extracted with Limma, global perturbations in known Gene Ontology (GO) terms and KEGG pathways were detected using the R/Bioconductor package GAGE (Luo et al., 2009) to test for changes in expression of the reported log 2 fold-changes reported by Limma in each term versus the background log 2 fold-changes of all genes found outside the respective term. The R/Bioconductor package heatmap3 (Zhao et al., 2014) and Pathview (Luo and Brouwer, 2013) was used to display heatmaps or annotated KEGG graphs across groups of samples for each GO term or KEGG pathway (respectively) with a Benjamini-Hochberg false-discovery rate adjusted p-value less than or equal to 0.05. In addition, GO term representation among significantly down-regulated and significantly up-regulated genes were determined using GO Consortium enrichment analysis tool (Ashburner et al., 2000; Mi et al., 2017; The Gene Ontology, 2017).

Mitochondria and bead uptake assays in BV2 cells—BV2 cells were washed in phosphate buffered saline (PBS) and treated with 0.05% trypsin-EDTA (Gibco) in PBS for 10-30 min. Cells were washed in 1 volume of BV2 Media, pelleted by centrifugation at 500 x *g* for 5 min at 4 °C, resuspended in 10 mL BV2 Media, and cell density was counted using a hemocytometer with 0.1% trypan blue. Aliquots of 1.0 x 10^5 BV2 cells were used for co-culture with purified mitochondria (2 μg, see below) or 1.0 μm red latex beads (100 beads per cell, or MOI 100, Fluoresbrite Polychromatic Red Microspheres, Polysciences, Inc.) in a volume of 200 μL/well in polystyrene tissue-culture treated 96-well round-bottom plates for 90 min at 37 °C and 5% CO_2. Cells were washed three times in 200 μL ice-cold BV2 Media and then twice in 200 μL ice-cold FACS Buffer (PBS with 2.5% heat-inactivated FBS and 2.5 mM EDTA) before flow cytometric analyses. In some experiments, purified mtD2

mitochondria were incubated with 1 mg/mL heparan sulfate proteoglycan (HSPG, Sigma-Aldrich) for 30 min at room temperature prior to co-culture with BV2 cells. In other experiments, BV2 cells were incubated with heparanases I, II, and III (5 U/mL each, New England Biolabs) in DMEM for 1 hour at 37 °C and 5% CO_2 prior to co-culture with purified mtD2 mitochondria._In some experiments, BV2 cells were stimulated with recombinant Interleukin (IL)-4 (20 ng/mL; R&D Systems) or recombinant interferon (IFN)-γ (10 ng/mL; R&D Systems) plus gamma-irradiated lipopolysaccharide (LPS, 1 ng/mL; Sigma-Aldrich) in BV2 Media for 24 hours prior to co-culture with 1 micron beads, purified mtD2 mitochondria, or being harvested in RLT Lysis Buffer for subsequent quantitative real-time polymerase chain reaction (PCR).

Quantitative real-time PCR—RNA was extracted from BV2 cells using the RNeasy Mini Kit (Qiagen) according to manufacturer instructions. Messenger (m)RNA was reverse transcribed using iScript Reverse Transcriptase Supermix (Biorad, cat no. 1708841). Expression of *Ext1, Ext2,* and *Hs6st1* was measured using TaqMan assays on a 7500 fast real-time PCR machine (Applied Biosystems).

Mitochondria isolation—Mitochondria were isolated using the Mitochondria Isolation Kit, Mouse Tissue (Miltenyi Biotec). mtDendra2 mice were euthanized, the right atrium was punctured, and the mouse was perfused with 10 mL PBS (sterile, ice-cold) via the left ventricle. Perfused liver was harvested, finely minced, and homogenized in a 2 mL dounce homogenizer in 1 mL Lysis Buffer with 7-8 strokes. Tissue homogenate was transferred to a 15 mL conical tube containing 9 mL 1X Separation Buffer (SB) and mixed thoroughly. Anti-TOM40 antibody conjugated to magnetic nanobeads (50 µL) was added and incubated in the dark at 4 °C with gentle rocking for 1 hour. The mixture was passed through a 30 µm nylon mesh and then an LS Column associated with a QuadroMACS magnet (Miltenyi Biotec). The column was washed 3 times with 3 mL of 1X SB. Purified mitochondria were eluted with 1.5 mL of 1X SB and pelleted by centrifugation at 15,000 x *g* for 2 min at 4 °C. The pellet was resuspended in 1 mL Storage Buffer (Miltenyi Biotec), pelleted again as above, resuspended in 1 mL Storage Buffer, and held on ice. Mitochondria protein concentration was determined using 10 µL of purified mitochondria and 300 µL Coomassie Plus Reagent (Pierce) alongside a standard curve of Bovine Serum Albumin (BSA, Piece). Absorbance was measured at 450 nm using a BioRad iMark Microplate Reader.

Brie CRISPR Library Preparation—Lentiviral libraries were synthesized, cloned, and produced as previously described (Doench et al., 2016). Cas9 activity was confirmed in stably-expressing BV2 cells (BV2-Cas9) using pXPR_011 (Addgene #59702) EGFP expression on a FACS Calibur instrument (BD Biosciences) (Orchard et al., 2016; Orvedahl et al., 2019). The lentiviral library was titered by transducing 3 x 10^6 BV2 cells with variable volumes of lentivirus (0, 10, 20, 40, 80, or 160 µl) in 2ml total volume of cell culture media in 50mL conical tubes. The cells were spinoculated for 2hr at 1000g at 30C. After spinoculation, cells were resuspended in cell culture media and 5 x 10^5 cells were plated per 15cm dish. Media was exchanged 48 hr later with D10 or puromycin (Puro)-containing media, and cells were counted 48-72 hours later. A standard curve was then interpolated to determine lentiviral concentration needed for transduction efficiency of 20-30%. For library

production, 1.6x10^8 BV2-Cas9 cells at 1.5x10^6 cells/mL were spinoculated with Brie lentivirus (Addgene #73633) sufficient to transduce 25% of cells. This was sufficient for 500x coverage for each of the approximately 80,000 sgRNAs. Following spinoculation, cells were resuspended, and plated at a density of 5 x 10^5 cells in 25 mL D10 in 15cm dishes. Forty-eight hours after transduction, media was exchanged with puromycin containing media and cells were cultured for an additional three days prior to pooling, aliquoting, and freezing in liquid nitrogen.

Genome-wide CRISPR knockout screen, sequencing, and analysis—An aliquot of 4 x 10^7 BV2-Brie cells were seeded in 20 x 150 mm tissue-culture treated dishes with 2 x 10^6 cells in 25 mL BV2 Media per dish and cultured for 48 hours, as described above. The cells were harvested as described above and counted using a hemocytometer. An aliquot of 1.5 x 10^8 cells were cultured in 150 mL of BV2 Media containing 6.0 mg (40 mg/mL) of purified mitochondria from livers of n=5 mtD2 mice for 90 min at 37 °C with gentle swirling each 15 min. Cells were pelleted by centrifugation at 500 x *g* for 5 min at 4 °C, washed in 50 mL of BV2 Media three times before washing once in 50 mL of PBS. Cells were stained with ZombieUV and rat anti-mouse F4/80-APC, as described above, in filter-sterilized FACS Buffer, and cells were sort-purified as described above. An aliquot of 1 x 10^7 cells was exposed to no mitochondria to determine a negative gate for sorting. The mitochondria-exposed pool of cells was held on ice, and mtD2-negative cells were sorted using an Aria I into sterile 2 mL sterile polypropylene tubes. Genomic DNA was isolated from the mtD2-negative BV2-Brie cells and an unsorted population 2 x 10^8 input cells using the QIAmp DNA Mini Kit according to manufacturer instructions.

Enrichment of sgRNA guides in mtD2-negative BV2 cells was determined by Illumina sequencing and STARS analysis, as previously described (Doench et al., 2016). Briefly, genomic DNA from mtD2-negative and input cells were aliquoted into multiple wells of 96-well plates with up to 10 μg DNA in a maximum 50 μL volume. Polymerase chain reaction (PCR) master mix (40 μL) containing ExTaq DNA polymerase (Clontech), ExTaq buffer, dNTP, P5 stagger primer, and water was added along with 10 μL of a barcoded primer, making a reaction volume of 100 μL. Samples were amplified with the following program: 95 °C (1 min) followed by 28 cycles of 94 °C for 30 sec, 52.5 °C for 30 sec, 72 °C for 30 sec, with a final 10 min a 72 °C. PCR product was purified with Agencourt AMPure XP SPRI beads per the manufacturer's protocol (Beckman Coulter). Samples were sequences on an Illumina HiSeq 2000. Barcodes in the P7 primer were de-convoluted and the sgRNA sequence was mapped to the reference of sgRNAs in the Brie library. To normalize for different numbers of reads per condition, read counts per sgRNA were normalized to 1 x 10^7 total reads per sample. This normalized value was then log-2 transformed. sgRNAs that were not sequenced were arbitrarily assigned a read count of 1. sgRNA frequencies were the analyzed using STARS software, which is available at http://www.broadinstitute.org/rnai/public/software/index (Doench et al., 2016). STARS computes a score for each gene of a rank-ordered sgRNA hits that was above 10% of total sequenced sgRNAs. A STAR score was only assigned to genes that scored above this threshold in at least two of the guides targeting that gene. In addition to the STAR score, we computed false discovery rates (FDR) to correct for multiple testing. FDR estimates the probability that the null hypothesis is true

(i.e., a gene is not a hit). Thus, the genes with the lowest FDRs are the most likely to be true hits.

Generation of BV2 knockout cells—Knockout (KO) cell lines in BV2 cells with lentiCRISPR v2 (Addgene #52961) lentivirus containing Cas9, a puromycin resistance gene, and the following CRISPR sgRNA guide sequences: *Hs6st1* (CGCCGGTCTTCTGGATGTGC); *Uxs1* (TCCACTTCCGAGGTATATGG); *Slc35b2* (CGGGTCTCCAGGTAAGAATA); *Papss1* (TGCTACACTTTGGATGGTGA); *Ugp2* (TCCAGGGCATGGAGATATCT); *B3gat3* (CTGGTCTCCTCTTTACACAC); *Extl3* (CGCGGCTCTTCGAGGCCCTG); *B4galt7* (CATCTATGTGCTCAACCAGG); *B3galt6* (CCGCGCTAAGGCCTTCCTGG); *Ext1* (CATGGAGTCCTGCTTCGATT); *Ext2* (CCCTGAGTACAGAGAGGAAC); and *Ugdh* (GCATTGTGCAGAACTCAAAT). As a control, sgRNA directed against *GFP* (GAAGTTCGAGGGCGACACCC) was used. Transduced cells were cultured at 37 °C and 5% CO_2 for 48 hours and then selected with puromycin (2.5 μg/mL) for 7 days. Clonal KO cell lines were generated by limiting dilution, and gene deletion was verified by deep sequencing. Clonal KO cells were propagated in BV2 Media, and aliquots of cells were frozen at −80 °C in heat-inactivated FBS containing 10% DMSO and stored at −80 °C till use. Thawed cells were plated in 150 mm dishes and cultured for 2 days to approximately 80% confluence, and aliquots of cells were co-cultured with purified mtD2 mitochondria or red latex beads, as described above. Flow cytometry was used to quantify the frequency of cells that were $mtD2^+$ or $bead^+$ using a BD X20 flow cytometer.

WAT co-culture system—WAT from donor CD45.1 or CD45.2 mtD2 mice fed a normal chow or HFD were co-cultured with equal masses of WAT form recipient congenically disparate CD45.1 or CD45.2 WT mice fed a chow or HFD. Equal masses of donor and recipient WAT (within 0.01-0.03 g) were finely minced together in DMEM containing 0.1% collagenase II at 37 °C for 120 min with rotation at 200 rpm at 45° angle. The SVF was isolated and stained for flow cytometric analyses, as described above. The frequency of recipient macrophages that were mtD2+ was quantified.

Quantification and Statistical Analysis

Statistical analyses—Data are expressed as mean ± standard error of the mean (SEM). Statistical significance for normally distributed data was determined using Student's t-tests for comparisons of 2 groups or analysis of variance (ANOVA) followed by Fisher LSD post-hoc tests for comparisons of 3 or more groups. For metabolic cage analyses, ANOVA with repeated measures and Fisher LSD post-hoc tests were used. Significance was set at $P<0.05$. Statistical analyses were performed with Prism 7 (GraphPad Software, Inc.), unless otherwise indicated.

Additional Resources

Not applicable

Supplementary Material

Refer to Web version on PubMed Central for supplementary material.

Acknowledgments:

This work was supported by National Institutes of Health (NIH) R01-DK111389, NIH Merit Award R37-AR046523, Shriner's Hospital for Children Grant #85400, and a grant from Siteman Cancer Center to S.L.T. Additional funding was provided by the NIH Office of the Director (DP5 OD028125), the Burroughs Wellcome Fund (CAMS 1019648), and Children's Discovery Institute (MI-F-2019-795) to J.R.B. Support was also provided by NIH R01-AI123348 (M.S.D.), K08-AR065577 (B.S.K.), R01-AR070116 (B.S.K.), Doris Duke Charitable Foundation (B.S.K.), Celgene Corporation (B.S.K.), LEO Pharma (B.S.K.), and K99-HL138163 (J.W.W.). The Genome Technology Access Center (GTAC) is partially supported by NCI Cancer Center Support Grant P30 CA91842 to Siteman Cancer Center, ICTS/CTSA Grant# UL1TR002345 from the National Center for Research Resources (NCRR), a component of the National Institutes of Health (NIH), and NIH Roadmap for Medical Research. We thank D. Brinja and E. Lantelme at the Flow Cytometry and Cell Sorting Core and E. Tycksen at GTAC at Washington University School of Medicine for their technical support.

REFERENCES:

Al Amir Dache Z, Otandault A, Tanos R, Pastor B, Meddeb R, Sanchez C, Arena G, Lasorsa L, Bennett A, Grange T, et al. (2020). Blood contains circulating cell-free respiratory competent mitochondria. FASEB J 34, 3616–3630. [PubMed: 31957088]

Ashburner M, Ball CA, Blake JA, Botstein D, Butler H, Cherry JM, Davis AP, Dolinski K, Dwight SS, Eppig JT, et al. (2000). Gene ontology: tool for the unification of biology. The Gene Ontology Consortium. Nat Genet 25, 25–29. [PubMed: 10802651]

Bosedasgupta S, and Pieters J (2014). Inflammatory stimuli reprogram macrophage phagocytosis to macropinocytosis for the rapid elimination of pathogens. PLoS Pathog 10, e1003879. [PubMed: 24497827]

Boudreau LH, Duchez AC, Cloutier N, Soulet D, Martin N, Bollinger J, Pare A, Rousseau M, Naika GS, Levesque T, et al. (2014). Platelets release mitochondria serving as substrate for bactericidal group IIA-secreted phospholipase A2 to promote inflammation. Blood 124, 2173–2183. [PubMed: 25082876]

Brestoff JR, and Artis D (2015). Immune regulation of metabolic homeostasis in health and disease. Cell 161, 146–160. [PubMed: 25815992]

Brestoff JR, Kim BS, Saenz SA, Stine RR, Monticelli LA, Sonnenberg GF, Thome JJ, Farber DL, Lutfy K, Seale P, et al. (2015). Group 2 innate lymphoid cells promote beiging of white adipose tissue and limit obesity. Nature 519, 242–246. [PubMed: 25533952]

Busse M, Feta A, Presto J, Wilen M, Gronning M, Kjellen L, and Kusche-Gullberg M (2007). Contribution of EXT1, EXT2, and EXTL3 to heparan sulfate chain elongation. J Biol Chem 282, 32802–32810. [PubMed: 17761672]

Caesar R, Reigstad CS, Backhed HK, Reinhardt C, Ketonen M, Lunden GO, Cani PD, and Backhed F (2012). Gut-derived lipopolysaccharide augments adipose macrophage accumulation but is not essential for impaired glucose or insulin tolerance in mice. Gut 61, 1701–1707. [PubMed: 22535377]

Camell CD, Sander J, Spadaro O, Lee A, Nguyen KY, Wing A, Goldberg EL, Youm YH, Brown CW, Elsworth J, et al. (2017). Inflammasome-driven catecholamine catabolism in macrophages blunts lipolysis during ageing. Nature 550, 119–123. [PubMed: 28953873]

Cani PD, Amar J, Iglesias MA, Poggi M, Knauf C, Bastelica D, Neyrinck AM, Fava F, Tuohy KM, Chabo C, et al. (2007). Metabolic endotoxemia initiates obesity and insulin resistance. Diabetes 56, 1761–1772. [PubMed: 17456850]

Chang JC, Chang HS, Wu YC, Cheng WL, Lin TT, Chang HJ, Kuo SJ, Chen ST, and Liu CS (2019). Mitochondrial transplantation regulates antitumour activity, chemoresistance and mitochondrial dynamics in breast cancer. J Exp Clin Cancer Res 38, 30. [PubMed: 30674338]

Chiu RW, Chan LY, Lam NY, Tsui NB, Ng EK, Rainer TH, and Lo YM (2003).Quantitative analysis of circulating mitochondrial DNA in plasma. Clin Chem 49, 719–726. [PubMed: 12709361]

Clemente-Postigo M, Oliva-Olivera W, Coin-Araguez L, Ramos-Molina B, Giraldez-Perez RM, Lhamyani S, Alcaide-Torres J, Perez-Martinez P, El Bekay R, Cardona F, et al. (2019). Metabolic endotoxemia promotes adipose dysfunction and inflammation in human obesity. Am J Physiol Endocrinol Metab 316, E319–E332. [PubMed: 30422702]

Court AC, Le-Gatt A, Luz-Crawford P, Parra E, Aliaga-Tobar V, Batiz LF, Contreras RA, Ortuzar MI, Kurte M, Elizondo-Vega R, et al. (2020). Mitochondrial transfer from MSCs to T cells induces Treg differentiation and restricts inflammatory response. EMBO Rep 21, e48052. [PubMed: 31984629]

Dobin A, Davis CA, Schlesinger F, Drenkow J, Zaleski C, Jha S, Batut P, Chaisson M, and Gingeras TR (2013). STAR: ultrafast universal RNA-seq aligner. Bioinformatics 29, 15–21. [PubMed: 23104886]

Doench JG, Fusi N, Sullender M, Hegde M, Vaimberg EW, Donovan KF, Smith I, Tothova Z, Wilen C, Orchard R, et al. (2016). Optimized sgRNA design to maximize activity and minimize off-target effects of CRISPR-Cas9. Nat Biotechnol 34, 184–191. [PubMed: 26780180]

Dong LF, Kovarova J, Bajzikova M, Bezawork-Geleta A, Svec D, Endaya B, Sachaphibulkij K, Coelho AR, Sebkova N, Ruzickova A, et al. (2017). Horizontal transfer of whole mitochondria restores tumorigenic potential in mitochondrial DNA-deficient cancer cells. Elife 6.

Ekre HP, Naparstek Y, Lider O, Hyden P, Hagermark O, Nilsson T, Vlodavsky I, and Cohen I (1992). Anti-inflammatory effects of heparin and its derivatives: inhibition of complement and of lymphocyte migration. Adv Exp Med Biol 313, 329–340. [PubMed: 1442268]

Flaherty SE 3rd, Grijalva A, Xu X, Ables E, Nomani A, and Ferrante AW Jr. (2019). A lipase-independent pathway of lipid release and immune modulation by adipocytes. Science 363, 989–993. [PubMed: 30819964]

Flegal KM, Kruszon-Moran D, Carroll MD, Fryar CD, and Ogden CL (2016). Trends in Obesity Among Adults in the United States, 2005 to 2014. JAMA 315, 2284–2291. [PubMed: 27272580]

Gemperle C, Schmid M, Herova M, Marti-Jaun J, Wuest SJ, Loretz C, and Hersberger M (2012). Regulation of the formyl peptide receptor 1 (FPR1) gene in primary human macrophages. PLoS One 7, e50195. [PubMed: 23185575]

Griessinger E, Moschoi R, Biondani G, and Peyron JF (2017). Mitochondrial Transfer in the Leukemia Microenvironment. Trends Cancer 3, 828–839. [PubMed: 29198439]

Hayakawa K, Esposito E, Wang X, Terasaki Y, Liu Y, Xing C, Ji X, and Lo EH (2016). Transfer of mitochondria from astrocytes to neurons after stroke. Nature 535, 551–555. [PubMed: 27466127]

He HQ, and Ye RD (2017). The Formyl Peptide Receptors: Diversity of Ligands and Mechanism for Recognition. Molecules 22.

Hotamisligil GS (2017). Inflammation, metaflammation and immunometabolic disorders. Nature 542, 177–185. [PubMed: 28179656]

Islam MN, Das SR, Emin MT, Wei M, Sun L, Westphalen K, Rowlands DJ, Quadri SK, Bhattacharya S, and Bhattacharya J (2012). Mitochondrial transfer from bone-marrow-derived stromal cells to pulmonary alveoli protects against acute lung injury. Nat Med 18, 759–765. [PubMed: 22504485]

Jackson MV, and Krasnodembskaya AD (2017). Analysis of Mitochondrial Transfer in Direct Co-cultures of Human Monocyte-derived Macrophages (MDM) and Mesenchymal Stem Cells (MSC). Bio Protoc 7.

Jiang D, Gao F, Zhang Y, Wong DS, Li Q, Tse HF, Xu G, Yu Z, and Lian Q (2016). Mitochondrial transfer of mesenchymal stem cells effectively protects corneal epithelial cells from mitochondrial damage. Cell Death Dis 7, e2467. [PubMed: 27831562]

Kalyanaraman B, Hardy M, Podsiadly R, Cheng G, and Zielonka J (2017). Recent developments in detection of superoxide radical anion and hydrogen peroxide: Opportunities, challenges, and implications in redox signaling. Arch Biochem Biophys 617, 38–47. [PubMed: 27590268]

Kim MJ, Hwang JW, Yun CK, Lee Y, and Choi YS (2018). Delivery of exogenous mitochondria via centrifugation enhances cellular metabolic function. Sci Rep 8, 3330. [PubMed: 29463809]

Kitani T, Kami D, Matoba S, and Gojo S (2014). Internalization of isolated functional mitochondria: involvement of macropinocytosis. J Cell Mol Med 18, 1694–1703. [PubMed: 24912369]

Larabee CM, Neely OC, and Domingos AI (2020). Obesity: a neuroimmunometabolic perspective. Nat Rev Endocrinol 16, 30–43. [PubMed: 31776456]

Lee KU, Lee HK, Koh CS, and Min HK (1988). Artificial induction of intravascular lipolysis by lipid-heparin infusion leads to insulin resistance in man. Diabetologia 31, 285–290. [PubMed: 3294068]

Lee YS, Wollam J, and Olefsky JM (2018). An Integrated View of Immunometabolism. Cell 172, 22–40. [PubMed: 29328913]

Liao Y, Smyth GK, and Shi W (2014). featureCounts: an efficient general purpose program for assigning sequence reads to genomic features. Bioinformatics 30, 923–930. [PubMed: 24227677]

Lin X, Wei G, Shi Z, Dryer L, Esko JD, Wells DE, and Matzuk MM (2000). Disruption of gastrulation and heparan sulfate biosynthesis in EXT1-deficient mice. Dev Biol 224, 299–311. [PubMed: 10926768]

Lindahl U, Couchman J, Kimata K, and Esko JD (2015). Proteoglycans and Sulfated Glycosaminoglycans In Essentials of Glycobiology. rd, Varki A, Cummings RD, Esko JD, Stanley P, Hart GW, Aebi M, Darvill AG, Kinoshita T, Packer NH, et al., eds. (Cold Spring Harbor (NY)), pp. 207–221.

Liu L, Yang X, Wang H, Cui G, Xu Y, Wang P, Yuan G, Wang X, Ding H, and Wang DW (2013). Association between variants of EXT2 and type 2 diabetes: a replication and meta-analysis. Hum Genet 132, 139–145. [PubMed: 23052945]

Liu R, Holik AZ, Su S, Jansz N, Chen K, Leong HS, Blewitt ME, Asselin-Labat ML, Smyth GK, and Ritchie ME (2015). Why weight? Modelling sample and observational level variability improves power in RNA-seq analyses. Nucleic Acids Res 43, e97. [PubMed: 25925576]

Luo W, and Brouwer C (2013). Pathview: an R/Bioconductor package for pathway-based data integration and visualization. Bioinformatics 29, 1830–1831. [PubMed: 23740750]

Luo W, Friedman MS, Shedden K, Hankenson KD, and Woolf PJ (2009). GAGE: generally applicable gene set enrichment for pathway analysis. BMC Bioinformatics 10, 161. [PubMed: 19473525]

Maeda A, and Fadeel B (2014). Mitochondria released by cells undergoing TNF-alpha-induced necroptosis act as danger signals. Cell Death Dis 5, e1312. [PubMed: 24991764]

Makki K, Froguel P, and Wolowczuk I (2013). Adipose tissue in obesity-related inflammation and insulin resistance: cells, cytokines, and chemokines. ISRN Inflamm 2013, 139239. [PubMed: 24455420]

McLaughlin T, Ackerman SE, Shen L, and Engleman E (2017). Role of innate and adaptive immunity in obesity-associated metabolic disease. J Clin Invest 127, 5–13. [PubMed: 28045397]

Mi H, Huang X, Muruganujan A, Tang H, Mills C, Kang D, and Thomas PD (2017). PANTHER version 11: expanded annotation data from Gene Ontology and Reactome pathways, and data analysis tool enhancements. Nucleic Acids Res 45, D183–D189. [PubMed: 27899595]

Mooij HL, Bernelot Moens SJ, Gordts PL, Stanford KI, Foley EM, van den Boogert MA, Witjes JJ, Hassing HC, Tanck MW, van de Sande MA, et al. (2015). Ext1 heterozygosity causes a modest effect on postprandial lipid clearance in humans. J Lipid Res 56, 665–673. [PubMed: 25568062]

Mousavi S, Moradi M, Khorshidahmad T, and Motamedi M (2015). Anti-Inflammatory Effects of Heparin and Its Derivatives: A Systematic Review. Adv Pharmacol Sci 2015, 507151. [PubMed: 26064103]

Oduah EI, Linhardt RJ, and Sharfstein ST (2016). Heparin: Past, Present, and Future. Pharmaceuticals (Basel) 9.

Ogden CL, Carroll MD, Lawman HG, Fryar CD, Kruszon-Moran D, Kit BK, and Flegal KM (2016). Trends in Obesity Prevalence Among Children and Adolescents in the United States, 1988–1994 Through 2013–2014. JAMA 315, 2292–2299. [PubMed: 27272581]

Orchard RC, Wilen CB, Doench JG, Baldridge MT, McCune BT, Lee YC, Lee S, Pruett-Miller SM, Nelson CA, Fremont DH, et al. (2016). Discovery of a proteinaceous cellular receptor for a norovirus. Science 353, 933–936. [PubMed: 27540007]

Orvedahl A, McAllaster MR, Sansone A, Dunlap BF, Desai C, Wang YT, Balce DR, Luke CJ, Lee S, Orchard RC, et al. (2019). Autophagy genes in myeloid cells counteract IFNgamma-induced TNF-mediated cell death and fatal TNF-induced shock. Proc Natl Acad Sci U S A 116, 16497–16506. [PubMed: 31346084]

Patro R, Duggal G, Love MI, Irizarry RA, and Kingsford C (2017). Salmon provides fast and bias-aware quantification of transcript expression. Nat Methods 14, 417–419. [PubMed: 28263959]

Patterson RE, Frank LL, Kristal AR, and White E (2004). A comprehensive examination of health conditions associated with obesity in older adults. Am J Prev Med 27, 385–390. [PubMed: 15556738]

Pham AH, McCaffery JM, and Chan DC (2012). Mouse lines with photo-activatable mitochondria to study mitochondrial dynamics. Genesis 50, 833–843. [PubMed: 22821887]

Pirzgalska RM, Seixas E, Seidman JS, Link VM, Sanchez NM, Mahu I, Mendes R, Gres V, Kubasova N, Morris I, et al. (2017). Sympathetic neuron-associated macrophages contribute to obesity by importing and metabolizing norepinephrine. Nat Med 23, 1309–1318. [PubMed: 29035364]

Pollara J, Edwards RW, Lin L, Bendersky VA, and Brennan TV (2018). Circulating mitochondria in deceased organ donors are associated with immune activation and early allograft dysfunction. JCI Insight 3.

Qiu Y, Nguyen KD, Odegaard JI, Cui X, Tian X, Locksley RM, Palmiter RD, and Chawla A (2014). Eosinophils and type 2 cytokine signaling in macrophages orchestrate development of functional beige fat. Cell 157, 1292–1308. [PubMed: 24906148]

Rao RR, Long JZ, White JP, Svensson KJ, Lou J, Lokurkar I, Jedrychowski MP, Ruas JL, Wrann CD, Lo JC, et al. (2014). Meteorin-like is a hormone that regulates immune-adipose interactions to increase beige fat thermogenesis. Cell 157, 1279–1291. [PubMed: 24906147]

Raoof R, van der Vlist M, Willemen HLDM, Prado J, Versteeg S, Vos M, Lockhorst R, Pasterkamp J, Khoury-Hanold W, Meyaard L, et al. (2020). Macrophages transfer mitochondria to sensory neurons to resolve inflammatory pain. bioRxiv.

Rebbeck CA, Leroi AM, and Burt A (2011). Mitochondrial capture by a transmissible cancer. Science 331, 303. [PubMed: 21252340]

Reilly SM, and Saltiel AR (2017). Adapting to obesity with adipose tissue inflammation. Nat Rev Endocrinol 13, 633–643. [PubMed: 28799554]

Ritchie ME, Phipson B, Wu D, Hu Y, Law CW, Shi W, and Smyth GK (2015). limma powers differential expression analyses for RNA-sequencing and microarray studies. Nucleic Acids Res 43, e47. [PubMed: 25605792]

Robinson MD, McCarthy DJ, and Smyth GK (2010). edgeR: a Bioconductor package for differential expression analysis of digital gene expression data. Bioinformatics 26, 139–140. [PubMed: 19910308]

Rutstein DD, Castelli WP, and Nickerson RJ (1969). Heparin and human lipid metabolism. Lancet 1, 1003–1008. [PubMed: 4181167]

Sasisekharan R, and Venkataraman G (2000). Heparin and heparan sulfate: biosynthesis, structure and function. Curr Opin Chem Biol 4, 626–631. [PubMed: 11102866]

Scozzi D, Ibrahim M, Liao F, Lin X, Hsiao HM, Hachem R, Tague LK, Ricci A, Kulkarni HS, Huang HJ, et al. (2019). Mitochondrial damage-associated molecular patterns released by lung transplants are associated with primary graft dysfunction. Am J Transplant 19, 1464–1477. [PubMed: 30582269]

Singer K, and Lumeng CN (2017). The initiation of metabolic inflammation in childhood obesity. J Clin Invest 127, 65–73. [PubMed: 28045405]

Sinha P, Islam MN, Bhattacharya S, and Bhattacharya J (2016). Intercellular mitochondrial transfer: bioenergetic crosstalk between cells. Curr Opin Genet Dev 38, 97–101. [PubMed: 27235808]

Sladek R, Rocheleau G, Rung J, Dina C, Shen L, Serre D, Boutin P, Vincent D, Belisle A, Hadjadj S, et al. (2007). A genome-wide association study identifies novel risk loci for type 2 diabetes. Nature 445, 881–885. [PubMed: 17293876]

Spees JL, Olson SD, Whitney MJ, and Prockop DJ (2006). Mitochondrial transfer between cells can rescue aerobic respiration. Proc Natl Acad Sci U S A 103, 1283–1288. [PubMed: 16432190]

Sun K, Kusminski CM, and Scherer PE (2011). Adipose tissue remodeling and obesity. J Clin Invest 121, 2094–2101. [PubMed: 21633177]

The Gene Ontology C (2017). Expansion of the Gene Ontology knowledgebase and resources. Nucleic Acids Res 45, D331–D338. [PubMed: 27899567]

Torralba D, Baixauli F, and Sanchez-Madrid F (2016). Mitochondria Know No Boundaries: Mechanisms and Functions of Intercellular Mitochondrial Transfer. Front Cell Dev Biol 4, 107. [PubMed: 27734015]

Wang L, Wang S, and Li W (2012). RSeQC: quality control of RNA-seq experiments. Bioinformatics 28, 2184–2185. [PubMed: 22743226]

Wellen KE, and Hotamisligil GS (2003). Obesity-induced inflammatory changes in adipose tissue. J Clin Invest 112, 1785–1788. [PubMed: 14679172]

Wu D, Molofsky AB, Liang HE, Ricardo-Gonzalez RR, Jouihan HA, Bando JK, Chawla A, and Locksley RM (2011). Eosinophils sustain adipose alternatively activated macrophages associated with glucose homeostasis. Science 332, 243–247. [PubMed: 21436399]

Wynn TA, Chawla A, and Pollard JW (2013). Macrophage biology in development, homeostasis and disease. Nature 496, 445–455. [PubMed: 23619691]

Zhao S, Gui Y, Sheng Q, and Shyr Y (2014). Advanced Heat Map and Clustering Analysis Using Heatmap3. BioMed Research International, 986048.

Zhu C, Xu P, He Y, Yuan Y, Wang T, Cai X, Yu L, Yang L, Wu J, Wang L, et al. (2017). Heparin Increases Food Intake through AgRP Neurons. Cell Rep 20, 2455–2467. [PubMed: 28877477]

Zhu L, Zhang J, Zhou J, Lu Y, Huang S, Xiao R, Yu X, Zeng X, Liu B, Liu F, et al. (2016). Mitochondrial transplantation attenuates hypoxic pulmonary hypertension. Oncotarget 7, 48925–48940. [PubMed: 27419637]

Highlights

1. Adipocytes transfer their mitochondria to macrophages *in vivo*
2. Mitochondria transfer from adipocytes to macrophages is decreased in obesity
3. Mitochondria uptake by macrophages is mediated by heparan sulfates
4. Mice that lack heparan sulfates on macrophages exhibit metabolic dysfunction

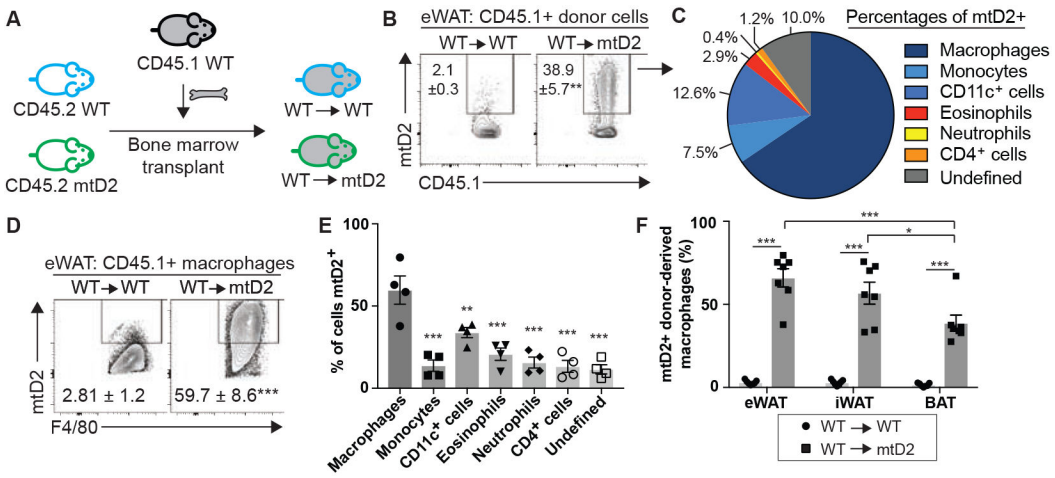

Figure 1. Macrophages acquire mitochondria from other cell types *in vivo*.

(A) Experimental design. **(B)** Frequency of live donor-derived WT immune cells that are mtD2$^+$ in recipient epididymal white adipose tissue (eWAT). Pre-gated on live CD45.1$^+$ CD45.2$^-$ cells. **(C)** Cell types represented within the population of WT donor cells that are mtD2$^+$. **(D)** Frequencies of WT donor-derived macrophages that are mtD2$^+$ in eWAT. Pre-gated on live CD45.1$^+$ CD45.2$^-$ CD64$^+$ F4/80$^+$ macrophages in eWAT. **(E)** Frequencies of the indicated donor-derived immune cells that are mtD2$^+$ in eWAT. **(F)** Frequencies of donor-derived macrophages that are mtD2+ in eWAT compared to inguinal (i)WAT and brown adipose tissue (BAT). Data represent 2-4 independent experiments with n=4-8 mice/group combined and are expressed as mean ± standard error of the mean (SEM). Student's t-tests (B and D), one-way ANOVA with Fisher's post-hoc test compared to macrophages (E), and two-way ANOVA with Fisher's post-hoc test (F), *P<0.05, **P<0.01, ***P<0.001. See also Supplemental Figure S1.

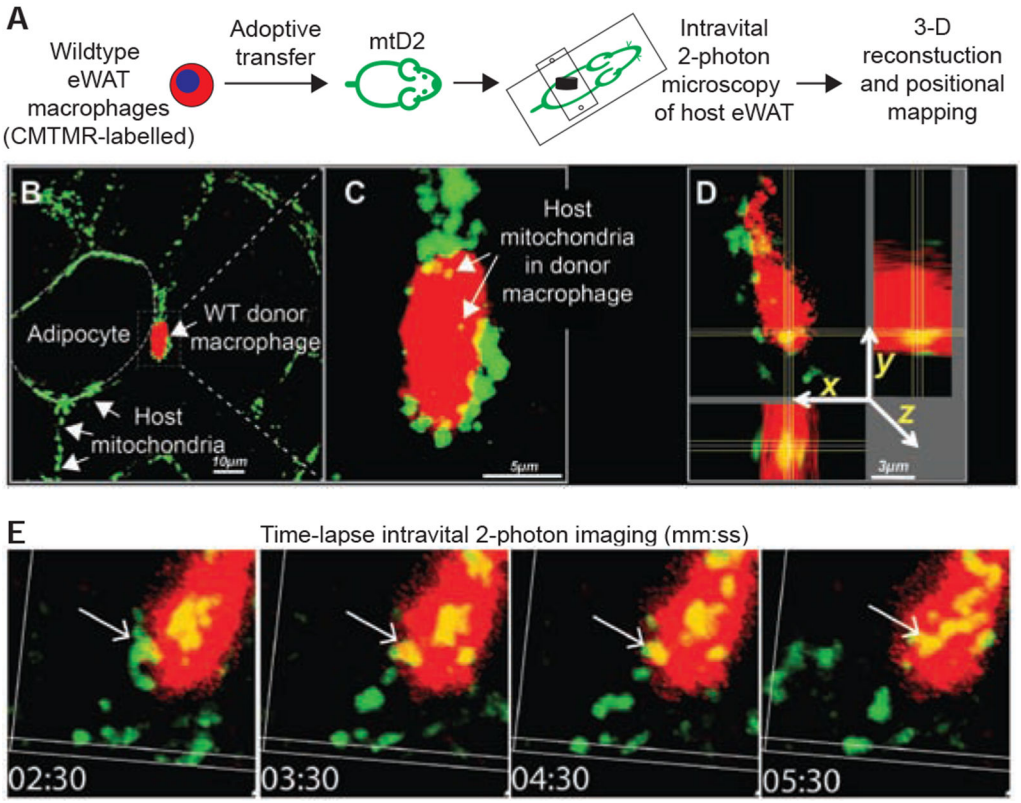

Figure 2. Intravital 2-photon microscopy reveals mitochondria transfer in white adipose tissue *in vivo*.

(A) Experimental design. **(B)** Low power magnification showing host adipocytes (dashed circular line), host-derived mtD2^{+} mitochondria (green, arrows), and a wildtype CMTMR-labelled macrophage (red). Scale bar, 10 μm. **(C)** High power magnification Z-stack of donor macrophage, showing yellow host-derived mitochondria within a donor macrophage (mac). Scale bar, 5 μm. **(D)** Three-dimensional reconstruction and positional mapping of host cell-derived mtD2^{+} mitochondria in a donor macrophage. Horizontal and vertical lines show coordinates. **(E)** Time lapse imaging revealing a mitochondria uptake event in WAT *in vivo*. Representative of n=4 mice from 2 independent experiments with n=2 mtD2 controls without adoptive transfer.

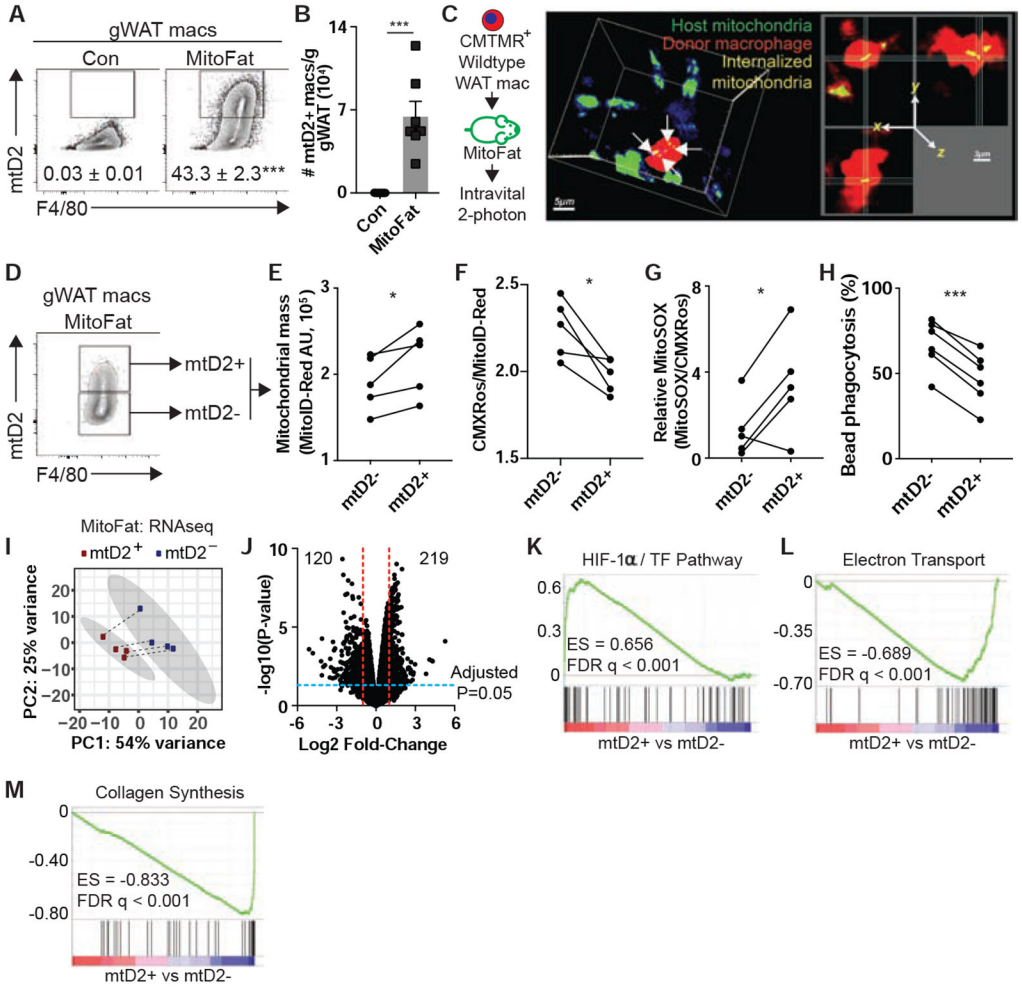

Figure 3. Adipocytes transfer mitochondria to macrophages in white adipose tissue *in vivo*, defining a distinct macrophage subpopulation.

(A) Frequencies and **(B)** numbers of live CD45$^+$ CD11b$^+$ CD64$^+$ macrophages per gram of eWAT from control (Con, n=9) and adipocyte-specific mitochondria reporter mice (MitoFat, n=7). **(C)** Wildtype eWAT macrophages (mac) were labelled with CMTMR and adoptively transfer into MitoFat mice for intravital 2-photon microscopy of host eWAT. Three-dimensional reconstruction (left) and positional mapping (right) of donor macrophage containing adipocyte-derived mitochondria (arrows). **(D)** Gating strategy to define macrophages that have (mtD2+) or have not (mtD2-) acquired mitochondria from adipocytes *in vivo* in MitoFat mice (n=5/group) for comparison of fluorescence intensity of **(E)** the charge-independent mitochondrial mass indicator MitoID-Red, **(F)** the charge-dependent mitochondria dye MitoTracker Red CMX Rosamine (CMXRos) normalized to MitoID-Red, **(G)** the charge-dependent dye MitoSOX Red normalized to CMXRos. **(H)** Comparison of mtD2+ and mtD2− eWAT macrophage phagocytosis of 1 μm polyred latex beads (n=6/group). For E-H, lines connect paired data points obtained from the same sample. **(I-L)** Messenger RNA sequencing of mtD2+ and mtD2− macrophages from eWAT of MitoFat mice (n=4). **(I)** Principal component analysis with dashed lines connecting paired samples from the same mouse and shaded ellipses defining 95% confidence intervals for each group.

(J) Volcano plot of detected transcripts. **(K-M)** Gene Set Enrichment Analyses showing enrichment of the HIF-1α/TF pathway (K) and de-enrichment of genes associated with electron transport (L) and collagen synthesis (M). Data expressed as mean ± standard error of the mean. Student's t-test (A-B) and paired t-test (E-H), *P<0.05, ***P<0.001. See also Supplemental Figure S2.

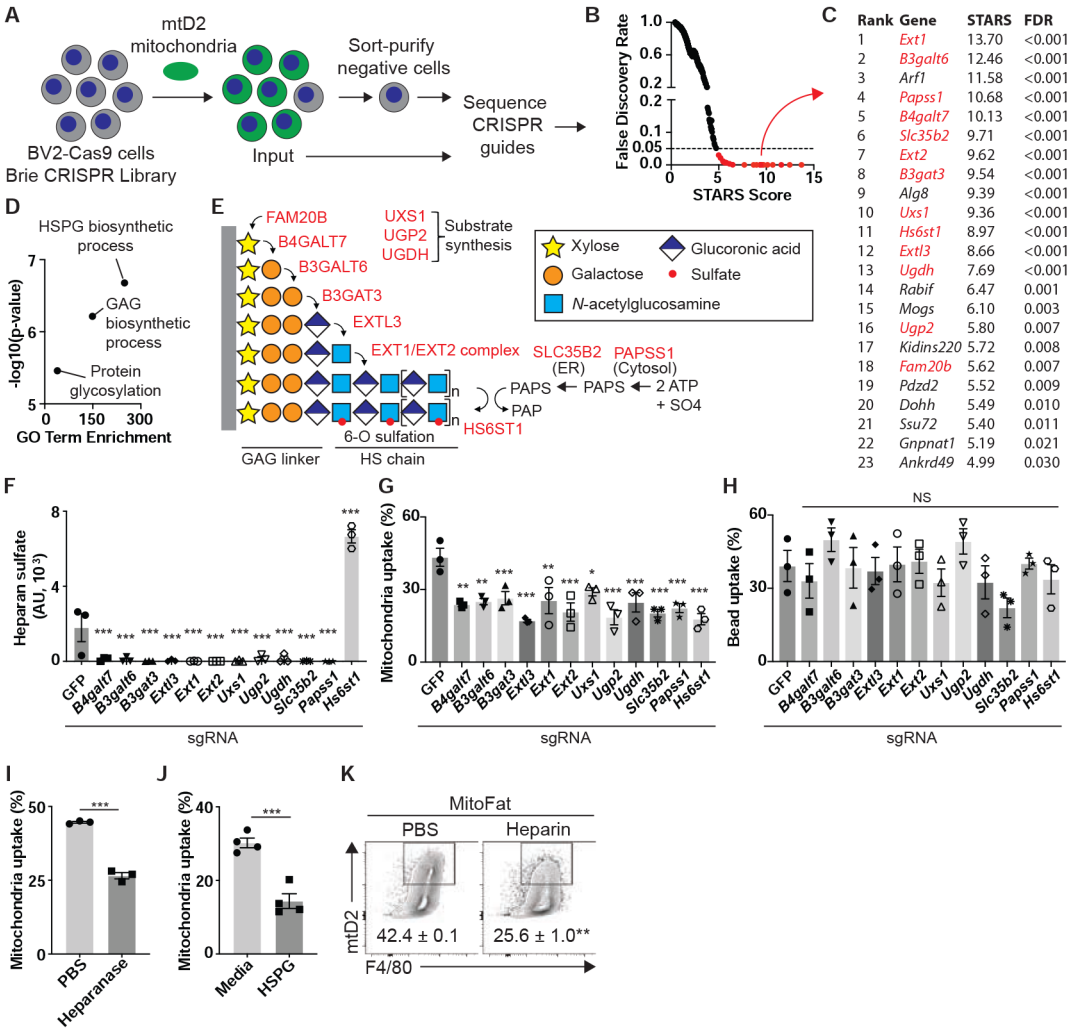

Figure 4. Genome-wide CRISPR knockout screen identifies heparan sulfates as essential for mitochondria uptake by macrophages.

(A) Experimental design of genome-wide CRISPR-Cas9 knockout screen. **(B)** STARS Score analyses identifies 23 enriched genes with false discovery rate (FDR) <0.05. **(C)** List of 23 enriched genes, of which red genes are required for heparan sulfate biosynthesis. **(D)** GO Term enrichment analysis of the 23 genes identified by the CRISPR screen. **(E)** Schematic relating the 13 heparan sulfate synthesis genes enriched in the CRISPR screen, tracing the entire HS biosynthesis pathway unsupervised. **(F)** Surface heparan sulfate levels, **(G)** mtD2 mitochondria uptake, and **(H)** 1 μm red latex bead phagocytosis in 13 clonally selected BV2-Cas9 cell lines, with sgRNA targeting the indicated genes. For F-H, n=3 independent experiments, one-way ANOVA with Dunnett post-hoc test comparing against the sgRNA to *Gfp* control, *P<0.05, **P<0.01, ***P<0.001. **(I)** Mitochondria uptake after pre-treating BV2 cells with heparanases I-III (5 U/mL each), n=3/group. **(J)** Mitochondria uptake by BV2 cells after pre-incubation of mtD2 mitochondria with 1 mg/mL heparan sulfate proteoglycan (HSPG), n=4/group. **(K)** Frequencies of mtD2^{+} macrophages in eWAT from MitoFat mice after 7 days of treatment with PBS or heparin (5 mg/kg, n=3/group). For I- K,

Student's t-test, ***P<0.001. *P<0.05, **P<0.01, ***P<0.001. For F-K, data are expressed as mean ± SEM. See also Supplemental Figure S4.

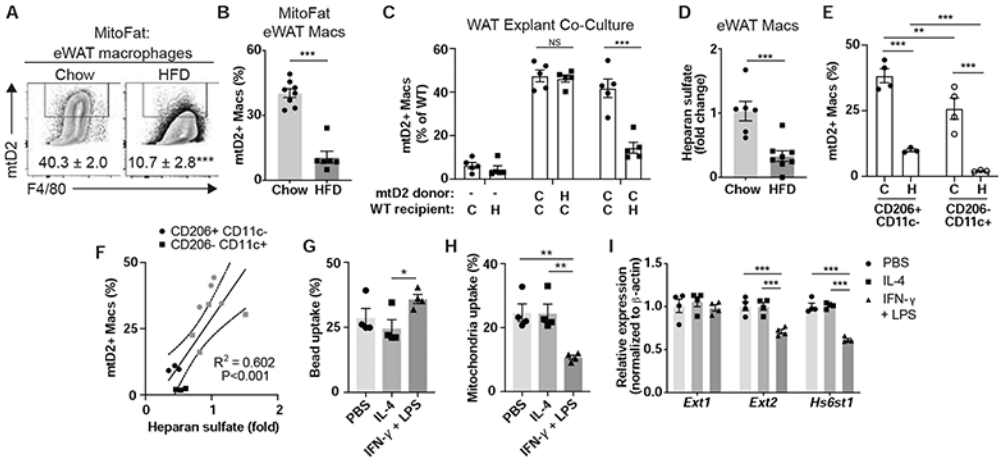

Figure 5. Intercellular mitochondria transfer to macrophages is impaired in obesity and following stimulation with IFN-γ and LPS.

(A-B) Male 6-week-old MitoFat mice were fed a chow or high fat diet (HFD) for 12 weeks, and live CD45$^+$ SiglecF$^-$ CD11b$^+$ CD64$^+$ macrophages in eWAT macrophages were identified by flow cytometry. The proportion of mtD2+ macrophages are shown. N=6-8/group from 3 independent experiments. **(C)** Frequency of WT recipient macrophages that are mtD2+ after WAT explant co-culture with congenically disparate mtD2 donor WAT. C, chow diet; H, high fat diet; n=5/group from 2 independent experiments combined. **(D)** Relative surface heparan sulfate levels on eWAT macrophages in mice fed a chow or HFD for 10-12 weeks, representative of n=6-8 mice/group pooled from 2 independent experiments. For A-D, Student's t-test, ***P<0.001. **(E)** Frequencies of mtD2+ cells in CD206$^+$ CD11c$^-$ and CD206$^-$ CD11c$^+$ macrophages from eWAT of MitoFat mice fed a chow (n=4) or HFD (n=3) for 12 weeks. **(F)** Pearson linear regression correlating the proportion of mtD2+ eWAT macrophages defined in panel E to their relative HS levels. Grey, chow; black, HFD. **(G-I)** BV2 cells were stimulated with phosphate buffered saline (PBS), 20 ng/mL interleukin (IL-4), or 10 ng/mL interferon (IFN)-γ plus 1 ng/mL lipopolysaccharide (LPS) for 24hr before co-culturing with 1 μm polyred latex beads and purified mtD2 mitochondria. Frequencies of cells that took up **(G)** beads and **(H)** mitochondria. **(I)** mRNA expression of the indicated HS biosynthesis genes in BV2 cells. For G-I, n=4 independent experiments, one-way ANOVA with Fisher's LSD post-hoc test. *P<0.05, **P<0.01, ***P<0.001. Data are represented as mean ± SEM. See also Supplemental Figure S5.

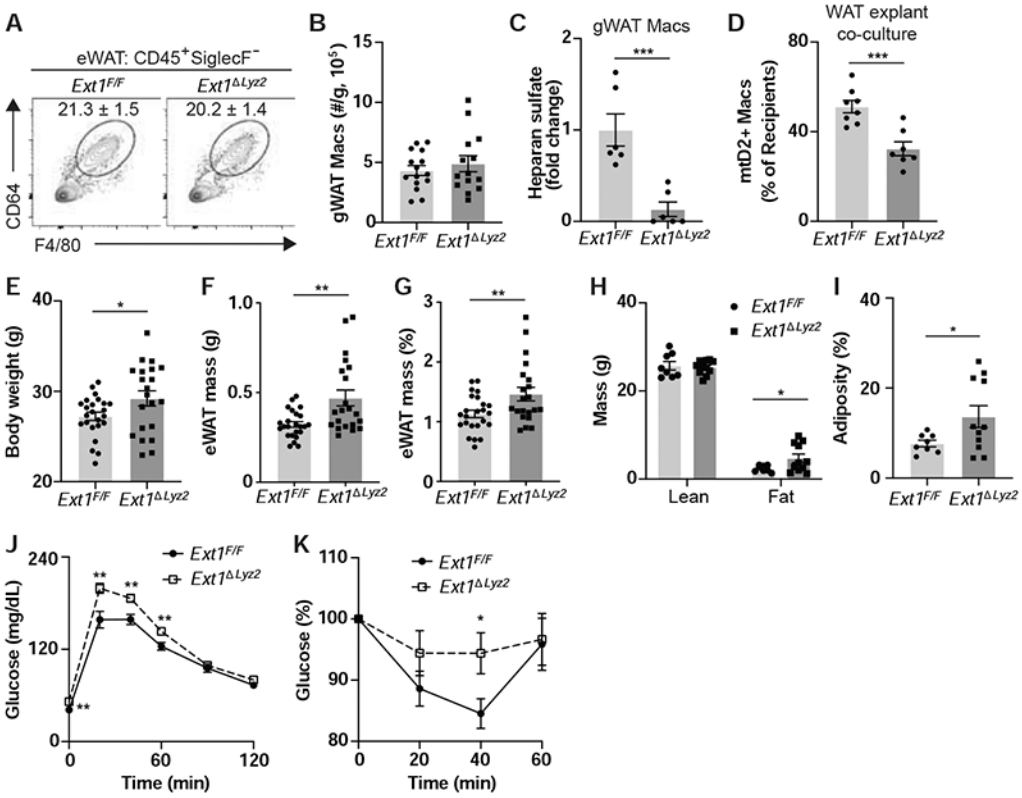

Figure 6. Genetic deletion of *Ext1* in myeloid cells impairs mitochondria transfer to macrophages and is associated with increased fat mass and glucose intolerance.

(A) Frequencies and **(B)** numbers per gram of eWAT macrophages in $Ext1^{\Delta Lyz2}$ mice (n=15) and $Ext1^{F/F}$ littermate controls (n=14) at steady state. Pre-gated on live $CD45^{+}$ $SiglecF^{-}$ cells. **(C)** Relative surface heparan sulfate levels on eWAT macrophages in $Ext1^{\Delta Lyz2}$ mice (n=6) and $Ext1^{F/F}$ littermate controls (n=6). **(D)** Frequencies of $Ext1^{\Delta Lyz2}$ (n=7) and $Ext1^{F/F}$ (n=8) eWAT recipient macrophages that are mtD2+ after eWAT explant co-culture with CD45.1 mtD2 donor WAT. **(E)** Body weight, **(F)** absolute eWAT mass, and **(G)** relative eWAT mass normalized to body weight in $Ext1^{\Delta Lyz2}$ mice (n=21) and $Ext1^{F/F}$ littermate controls (n=24). **(H)** Whole body lean and fat masses, **(I)** adiposity, **(J)** glucose tolerance tests, and **(K)** insulin tolerance tests in 5-6-month-old $Ext1^{\Delta Lyz2}$ mice (n=8) and $Ext1^{F/F}$ littermate controls (n=11). For A-I, Student's t-test. For J-K, two-way ANOVA with repeated measures with Fisher's LSD post-hoc test. *P<0.05, **P<0.01, ***P<0.001. Data are represented as mean ± SEM.

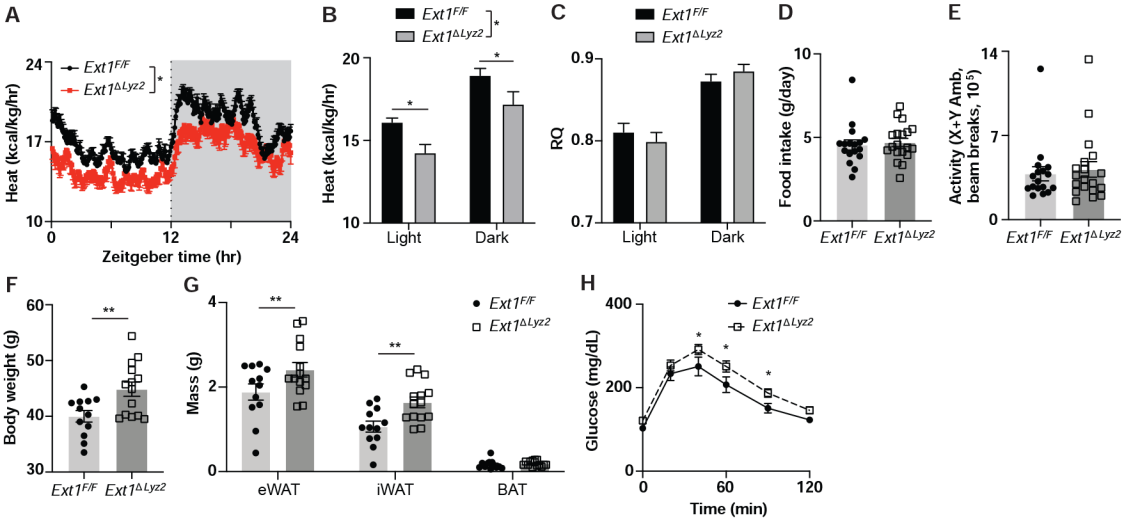

Figure 7. Deletion of *Ext1* in myeloid cells is associated with decreased energy expenditure and increased susceptibility to diet-induced obesity.

(A-E) Metabolic cage analyses of $Ext1^{\Delta Lyz2}$ mice (n=19) and $Ext1^{F/F}$ littermate controls (n=17). Energy expenditure expressed as heat produced per kg/body weight per hr at **(A)** 5.5 min resolution and **(B)** on average for light vs dark phases. **(C)** Respiratory quotient (RQ) during the light vs dark phases. **(D)** Food intake and **(E)** physical activity levels. **(F)** Body weight, **(G)** indicated adipose tissue depot masses, and **(H)** glucose tolerance tests of 5-6-month old $Ext1^{\Delta Lyz2}$ mice (n=14) and $Ext1^{F/F}$ littermate controls (n=12) fed a HFD for 9 weeks. For A-C and H, two-way ANOVA with repeated measures and LSD post-hoc test. For D-F, Student's t-test. For G, two-way ANOVA with LSD post-hoc test. *P<0.05, **P<0.01. Data are represented as mean ± SEM.

Key Resources Table

REAGENT or RESOURCE	SOURCE	IDENTIFIER
Antibodies		
Anti-F4/80 MicroBeads UltraPure, mouse	Miltenyi Biotec	Cat#130-110-443
Anti-HS IgM (clone F58-10E4)	Amsbio	Cat#370255-1
Anti-mouse IgM-PE/Cy7 (clone RMM-1)	BioLegend	Cat#406514
Mouse anti-mouse CD64-PE-Dazzle594 (clone X54-5/7.1)	BioLegend	Cat#139304
Rat anti-mouse CD16/32 (clone 2.4G2)	BD Biosciences	Cat#553142
Rat anti-mouse CD206-PE/Cy7 (clone C068C2)	BioLegend	Cat#141720
Rat anti-mouse CD4-APC/Fire750 (clone RM4-5)	BioLegend	Cat#100568
Rat anti-mouse CD45-BUV395 (clone 30-F11)	BD Horizon	Cat#564279
Rat anti-mouse CD45.1-APC (clone A20)	BioLegend	Cat#110714
Rat anti-mouse CD45.2-BUV395 (clone 104)	BD Horizon	Cat#564616
Rat anti-mouse F4/80-APC (clone BM8)	BioLegend	Cat#123116
Rat anti-mouse iNOS-PE/Cy7 (clone CXNFT)	ThermoFisher/eBioscience	Cat#25-5920-82
Rat anti-mouse Ly6C-BV510 (clone HK1.4)	BioLegend	Cat#128033
Rat anti-mouse Ly6G-BV785 (clone 1A8)	BioLegend	Cat#127645
Rat anti-mouse SiglecF-BV421 (clone E50-2440)	BD Pharmingen	Cat#562681
Rat anti-mouse SiglecF-PE (clone E50-2440)	BD Pharmingen	Cat#552126
Rat anti-mouse/human ARG1-APC (clone A1exF5)	ThermoFisher/eBioscience	Cat#17-3697-82
Rat anti-mouse/human CD11b-BV650 (clone M1/70)	BioLegend	Cat#101259
Rat IgG2a kappa-APC (clone BR2a)	ThermoFisher/eBioscience	Cat#17-4321-81
Rat IgG2a kappa-PE/Cy7 (clone eBR2a)	ThermoFisher/eBioscience	Cat#25-4321-82
Rat-anti-mouse F4/80-PE (clone BM8)	BioLegend	Cat#123110
Bacterial and Virus Strains		
pXPR_011	Addgene	#59702
Mouse CRISPR Knockout Pooled Library (Brie) lentivirus	Addgene	#73633
lentiCRISPR v2	Addgene	#52961
Chemicals, Peptides, and Recombinant Proteins		
60% high fat diet, irradiated	Research Diets, Inc.	Cat#D12492i
ACK Red Blood Cell Lysis Buffer	Gibco	Cat#A10492-01
Agencourt AMPure XP SPRI beads	Beckman Coulter	Cat#A63881
Bovine Serum Albumin	Pierce	Cat#23209
Brilliant Stain Buffer	BD Horizon	Cat#566349
CMTMR	ThermoFisher	Cat#C2927
Collagenase type II	Sigma-Aldrich	Cat#C6885
Contour handheld glucometer	Bayer	Cat#9545C
Coomassie Plus Reagent	Pierce	Cat#23236
Delbuco’s Modified Eagle Media (DMEM) with 4.5 g/L D-glucose, L-glutamine, and no sodium pyrophosphate	Gibco	Cat#11965-084

REAGENT or RESOURCE	SOURCE	IDENTIFIER
Antibodies		
DPBS	Gibco	Cat#14190-136
EDTA, 0.5M, pH 8.0	Invitrogen	Cat#AM9260G
ExTaq DNA polymerase	Clontech / Takara	Cat#RR001C
Fetal bovine serum (FBS)	Corning	Cat#35-010-CV
Fluoresbrite Polychromatic Red Microspheres, 1 micron	Polysciences, Inc.	Cat#18660-5
Glucose	Sigma-Aldrich	Cat#G7528
Grade I-A unfractionated heparin sodium salt, BioReagent	Sigma-Aldrich	Cat#H3149
Heparan sulfate proteoglycan	Sigma-Aldrich	Cat#H4777
Heparanase I	New England Biolabs	Cat#P0735S
Heparanase II	New England Biolabs	Cat#P0736L
Heparanase III	New England Biolabs	Cat#P0737L
Humulin R	Lilly	Cat#0002-8215-17
L-glutamine	Corning	Cat#25-005-Cl
Lipopolysaccharide from E. coli O111:B4, BioXtra	Sigma-Aldrich	Cat#L4391-1MG
MitoID-Red	Enzo Life Sciences	Cat#ENZ-51007-500
MitoSOX Red	ThermoFisher	Cat#M36008
MitoTracker Red CMXRos	ThermoFisher	Cat#M7512
Penicillin-Streptomycin	Corning	Cat#30-002-Cl
Puromycin	Gibco	Cat#A11138-03
Recombinant murine IFN-γ	R&D Systems	Cat#485-MI-100
Recombinant murine IL-4	R&D Systems	Cat#404-ML-100
Trypan blue	Sigma-Aldrich	Cat#T8154
Trypsin-EDTA	Gibco	Cat#15400-054
Ultracomp eBeads Compensation Beads	Invitrogen	Cat#01-2222-42
ZombieUV Fixable Viability Dye	BioLegend	Cat#423108
Critical Commercial Assays		
Cytofix/Cytoperm	BD Biosciences	Cat#554714
Mitochondria Isolation Kit, Mouse Tissue	Miltenyi Biotec	Cat#130-096-946
RNeasy Micro kit	Qiagen	Cat#74004
RNeasy Mini kit	Qiagen	Cat#74106
QIAmp DNA Mini Kit	Qiagen	Cat#51306
Deposited Data		
RNAseq dataset comparing mtD2− and mtD2+ macrophages from eWAT of MitoFat mice	GEO Database	GSE157462
Experimental Models: Cell Lines		
BV2 cells	Orchard et al., 2016	n/a
Experimental Models: Organisms/Strains		
Adipoq$^{Cre/+}$	Jackson Labs	Stock no. 28020
C57BL/6J	Jackson Labs	Stock no. 664

REAGENT or RESOURCE	SOURCE	IDENTIFIER
Antibodies		
CD45.1 (*Ptprc*^{a})	Jackson Labs	Stock no. 2014
Ext1$^{Flox/Flox}$	Jackson Labs	Stock no. 9326
Ext1$^{Flox/Flox}$;*Lyz2Cre*$^{+/-}$	Generated in house	n/a
Fpr1$^{-/-}$	Jackson Labs	Stock no. 32933
Fpr1$^{-/-}$ MitoFat	Generated in house	n/a
Lyz2$^{Cre/+}$	Jackson Labs	Stock no. 4781
MitoFat (*mtD2*$^{Flox/+}$;*Adipoq*$^{Cre/+}$)	Generated in house	n/a
mtDendra2 (i.e., PhAM, mtD2)	Jackson Labs	Stock no. 18397
mtDendra2$^{Flox/+}$ (i.e., PhAM Flox, mtD2$^{Flox/+}$)	Jackson Labs	Stock no. 18385
Oligonucleotides		
sgRNA targeting *B3galt6*: CCGCGCTAAGGCCTTCCTGG	Integrated DNA Technologies	n/a
sgRNA targeting B3gat3: CTGGTCTCCTCTTTACACAC	Integrated DNA Technologies	n/a
sgRNA targeting B4galt7: CATCTATGTGCTCAACCAGG	Integrated DNA Technologies	n/a
sgRNA targeting Ext1 CATGGAGTCCTGCTTCGATT	Integrated DNA Technologies	n/a
sgRNA targeting Ext2 CCCTGAGTACAGAGAGGAAC	Integrated DNA Technologies	n/a
sgRNA targeting Extl3 CGCGGCTCTTCGAGGCCCTG	Integrated DNA Technologies	n/a
sgRNA targeting Gfp GAAGTTCGAGGGCGACACCC	Integrated DNA Technologies	n/a
sgRNA targeting Hs6st1 CGCCGGTCTTCTGGATGTGC	Integrated DNA Technologies	n/a
sgRNA targeting Papss1 TGCTACACTTTGGATGGTGA	Integrated DNA Technologies	n/a
sgRNA targeting Slc35b2 CGGGTCTCCAGGTAAGAATA	Integrated DNA Technologies	n/a
sgRNA targeting Ugdh GCATTGTGCAGAACTCAAAT	Integrated DNA Technologies	n/a
sgRNA targeting Ugp2 TCCAGGGCATGGAGATATCT	Integrated DNA Technologies	n/a
sgRNA targeting Uxs1: TCCACTTCCGAGGTATATGG	Integrated DNA Technologies	n/a
TaqMan Gene Expression Assay Beta-actin FAM	Applied Biosystems	Mm00607939_s1
TaqMan Gene Expression Assay Ext1 FAM	Applied Biosystems	Mm00468769_m1
TaqMan Gene Expression Assay Ext2 FAM	Applied Biosystems	Mm00468775_m1
TaqMan Gene Expression Assay Hs6st1 FAM	Applied Biosystems	Mm01229698_s1
Software and Algorithms		
Prism 7	GraphPad Software, Inc.	n/a
OxyMax	Columbus Instruments	n/a
STARS software	http://www.broadinstitute.org/rnai/public/software/index (Doench et al., 2016)	n/a
STAR version 2.0.4b	(Dobin et al., 2013).	n/a
Subread:featureCount v1.4.5	(Liao et al., 2014).	n/a
Sailfish version 0.6.13	(Patro et al., 2017).	n/a
RSeQC version 2.3	(Wang et al., 2012).	n/a
R/Bioconductor package EdgeR	(Robinson et al., 2010)	n/a

REAGENT or RESOURCE	SOURCE	IDENTIFIER
Antibodies		
Limma	(Ritchie et al., 2015)	n/a
voomWithQualityWeights	(Liu et al., 2015).	n/a
GAGE	(Luo et al., 2009)	n/a
heatmap3	(Zhao et al., 2014)	n/a
Pathview	(Luo and Brouwer, 2013)	n/a
GO Consortium enrichment analysis tool	(Ashburner et al., 2000; Mi et al., 2017; The Gene Ontology, 2017)	n/a
Imaris software	BITPLANE, Inc.	n/a
FlowJo v10	FlowJo, LLC	n/a